


Article

CFD Simulation of Centrifugal Pump with Different Impeller Blade Trailing Edges

Hui Li ¹, Yongjun Chen ², Yang Yang ³, Shixin Wang ¹, Ling Bai ¹ and Ling Zhou ^{1,*} 

¹ National Research Center of Pumps, Jiangsu University, Zhenjiang 212013, China

² Shanghai Panda Machinery (Group) Co., Ltd., Shanghai 201704, China

³ College of Hydraulic Science and Engineering, Yangzhou University, Yangzhou 225009, China

* Correspondence: lingzhou@ujs.edu.cn

Abstract: The centrifugal pump is one of the most widely used types of power machinery in the field of ship and ocean engineering, and the shape of the impeller blade trailing edge has an important influence on their performance. To reveal the mechanism of the effect of different trailing edges on external performance, the internal flow of 16 types of impeller blade trailing edges of a centrifugal pump, consisting of Bezier trailing edges, rounding on the pressure side, cutting on the suction side, and the original trailing edge is studied by numerical simulation. The reverse flow, shaft power, and energy loss distribution in the impeller and diffuser along the streamwise direction are analyzed by calculating them on each micro control body sliced from the fluid domain. The entropy production theory and Ω -vortex identification method are used to display the magnitude and location of energy loss and the vortex structure. Finally, a static structural analysis of the impeller with different trailing edges is performed. The results show that different impeller trailing edges can clearly affect the efficiency of the pump, i.e., the thinner the trailing edge, the higher the efficiency, with the thickest model reducing efficiency by 5.71% and the thinnest model increasing efficiency by 0.59% compared to the original one. Changing the shape of the impeller trailing edge has a great influence on the reverse flow, shaft power, and energy loss near the impeller trailing edge and diffuser inlet but has little influence on the leading part of the impeller. The distribution of local entropy production rate, energy loss, and reverse flow along the streamwise direction shows similar rules, with a local maximum near the leading edge of the impeller due to the impact effect, and a global maximum near the impeller trailing edge resulting from strong flow separation and high vortex strength due to the jet-wake flow. Thinning the impeller trailing edge and smoothing its connection with the blade can reduce the vortex strength and entropy production near the impeller trailing edge and diffuser inlet, improve the flow pattern, and reduce energy loss, thus improving the pump efficiency. In all models, the maximum equivalent stress is less than 6.5 MPa and the maximum total deformation is less than 0.065mm. The results are helpful for a deeper understanding of the complex flow mechanism of the centrifugal pump with different blade trailing edges.

Keywords: centrifugal pump; blade trailing edge; Bezier curve; internal flow; entropy production; Ω -vortex identification



Citation: Li, H.; Chen, Y.; Yang, Y.; Wang, S.; Bai, L.; Zhou, L. CFD Simulation of Centrifugal Pump with Different Impeller Blade Trailing Edges. *J. Mar. Sci. Eng.* **2023**, *11*, 402. <https://doi.org/10.3390/jmse11020402>

Academic Editor: Spyros A. Mavrakos

Received: 16 January 2023

Revised: 4 February 2023

Accepted: 9 February 2023

Published: 11 February 2023



Copyright: © 2023 by the authors. Licensee MDPI, Basel, Switzerland. This article is an open access article distributed under the terms and conditions of the Creative Commons Attribution (CC BY) license (<https://creativecommons.org/licenses/by/4.0/>).

1. Introduction

The centrifugal pump, which converts mechanical energy into kinetic and pressure energy when fluid rotates in an impeller, is one of the most popular and important fluid-conveying equipment in the field of ocean engineering [1–3]. The impeller plays the most important role among all pump components [4]. According to Euler's turbine equation and the velocity triangle, the performance of the impeller is mainly determined by the inlet and outlet flow state [5]. Usually, the inflow of the impeller is without pre-swirl, so the performance of the pump is mainly affected by the outflow of the impeller.

A small change in the blade trailing edge (BTE) can cause a large change in pump performance [6]; therefore, it is an easy, economical, and effective method to improve

pump performance. Kikuyama, et al. [6] studied the influence of cutting the BTE on the performance of a centrifugal pump and found that when the BTE on the pressure side (PS) was cut with a constant angle, the head would decrease with a small cutting amount, and then would gradually increase as the cutting amount increased. When the BTE on the suction side (SS) was cut with a constant angle, the head would always increase with the increase in the cutting amount. Wu et al. [7] rounded the SS of the BTE of a mixed-flow pump with different radii. Their results showed that as the radius of the rounding increased, the head curve became flatter, and the efficiency was improved. The modification of the BTE effectively improved the head and efficiency for large flow rates. Warda et al. [8] numerically investigated the effect of different BTE shapes on the performance of a low specific speed centrifugal pump and showed that a V-cut profile, circular profile, and ellipse on the PS could reduce the vortex intensity and improve the head and efficiency compared to an ordinary BTE. Litfin et al. [9] compared the effects of three different BTEs, namely, the default, straight-cut, and under-filed, on the performance of wastewater pumps by numerical calculations and experimental studies and analyzed the effects of different BTEs on the flow losses in different sections of the impeller.

The shape of a BTE can change the distribution of the pressure and velocity at the impeller outlet and affect the jet-wake structure [10], thus affecting the unsteady pressure pulsation caused by the rotor-stator interaction, which leads to fluid-induced vibration and noise [11]. Many scholars have studied the influence of the BTE on the unsteady performance of a pump. Al-Qutub et al. [12] investigated the effect of a V-shaped cut at the impeller BTE on the performance, pressure pulsation, and vibration of a double suction pump and showed that the V-cut BTE could reduce the pressure pulsation and vibration of the pump with a slight reduction in the head. Gao et al. [11] and Zhang et al. [13] studied the effect of different BTEs on the performance and pressure pulsation of a low specific speed centrifugal pump by large eddy simulation. The results showed that an ellipse on the PS and an ellipse on both sides could clearly increase the pump efficiency and reduce the pressure pulsation. Cui et al. [14] investigated the effect of different cutting angles of the straight blade trailing edge on the external characteristics, unsteady flow, and vibration using numerical and experimental methods, and the results showed that 30- and 45-degree cutting angles can slightly increase the pump head and efficiency and reduce the pressure pulsation, vibration displacement, and vibration energy in the volute. Mansour et al. [15] used numerical calculations and a high-speed camera to compare the effects of a round BTE and trimmed BTE on the performance and flow regime of a single-phase and air-water two-phase flow in a centrifugal pump, showing that the round BTE provided better performance than the trimmed BTE in both the single and two-phase flow. According to the study by Huang et al. [1], cutting the BTE on the PS to reduce the outlet angle could increase the pump head and efficiency, reduce the velocity in the jet zone of the PS near the impeller outlet, improve the uniformity of the Euler head distribution, and reduce the intensity of pressure pulsation. Lin et al. [16] and Lin et al. [17] investigated the effect of a bionic sinusoidal trailing edge on the pressure pulsation and energy loss of a centrifugal pump, and their results showed that a reasonably designed bionic trailing edge can effectively reduce pressure pulsation and internal flow loss. In addition, blade thickness [18,19] and modification of the blade on the PS [10,20,21] have effects on pump performance and pressure pulsation. This research shows that a reasonable design can reduce energy loss, improve the uniformity of velocity and pressure distribution at the impeller outlet, reduce the secondary flow and suppress jet-wake structure, and improve internal flow, thus improving pump performance and reducing pressure pulsation and vibration.

The above studies mainly use lines, arcs, or ellipses to modify the BTE, though it can be difficult to achieve a flexible and diversified modification, however, the Bezier curve can easily modify the BTE. The Bezier curve was proposed by Pierre Bezier in 1962 to design the body of a car [22]. By adjusting the control points, the shape of the Bezier curve can be easily changed, and the direction of the start and end points can be effectively controlled;

additionally, it has continuous curvature so that it can be smoothly connected with other curves. Bezier curves are widely used in engineering applications such as mechanical design and computer graphics [23]. It can also be used in fluid dynamic designs, such as airfoil design [24], turbine blade design on the PS and SS [25], and the optimization design of a pump meridian section [26]. However, to the best of our knowledge, there are no studies using Bezier curves to modify the BTE of centrifugal pumps. In addition, the effect of different BTEs on the magnitude and location of energy loss in a pump has rarely been studied.

Aiming to study the effect of different BTEs on the performance and internal flow of a centrifugal pump, this paper adopts the Bezier curve, rounding on the PS, or cutting on the SS to modify the BTE. Firstly, the simulation results are verified by experiments. Then, the relationships between the efficiency and flow pattern of impeller outlet for different BTE models at a nominal flow rate are compared by simulation. The reverse flow and the distribution of shaft power and energy loss within the impeller and diffuser along the streamwise direction are then analyzed. Entropy production methods and Ω -vortex identification are used for four typical BTE models to show the magnitude and location of energy loss and the vortex structure. Finally, a one-way fluid-structure interaction is used to analyze the strength of the impeller with different BTEs. The findings reveal the mechanism of the effect of different BTEs on the internal flow in the impeller and diffuser at a nominal flow rate and can be referred to as the design of the impeller BTE.

2. Geometry Model

In this study, a centrifugal pump with a diffuser is investigated with rated flow rate $Q_d = 14 \text{ m}^3/\text{h}$, rated head $H_d = 14 \text{ m}$, rotating speed $n_d = 2850 \text{ rpm}$, and specific speed $n_s = 3.65n \cdot Q^{0.5}/H^{0.75} = 89.6$ [27]. The main design parameters are shown in Table 1. To study the influence of the impeller BTE on pump performance, a 4th-order of Beizer curve, rounding on the PS of the BTE with different radii, and cutting on the PS of the BTE with different angles are applied to modify the impeller BTE. There are a total of 16 BTE models, including the original one.

Table 1. Main design parameters of the centrifugal pump.

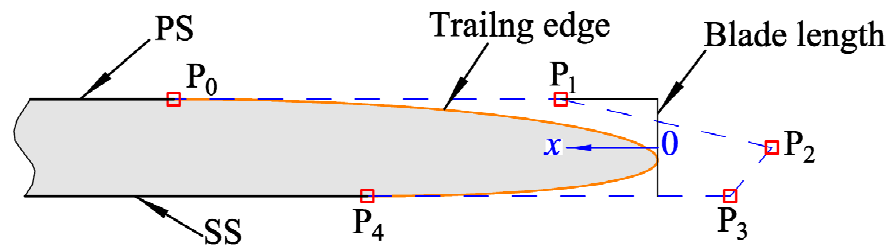
Parameters	Value
Rated rotating speed n_d , r/min	2850
Rated flow rate Q_d , m^3/h	14
Rated head H_d , m	14
Specific speed n_s	89.6
Number of impeller blades, Z_{La}	6
Number of diffuser vanes, Z_{Le}	7
Impeller inlet diameter D_1 , mm	48
Impeller outlet diameter D_2 , mm	116.6
Impeller outlet width b_2 , mm	7.8

As shown in Figure 1a, the 4th-order Bezier curve controlled by five points from P_0 – P_4 is plotted by Equation (1). P_0 is the intersection of the PS and the BTE, and P_4 is the intersection of the SS and the BTE; they can move along the blade surface. To make sure that the BTE is smoothly connected to the blade surface, P_1 and P_3 can only move along the tangent direction of P_0 and P_4 , respectively. The vertical position of P_2 is fixed on the meanline of the blade, and its horizontal position is automatically adjusted so that the BTE is aligned with the blade length. With the blade length as the zero point and horizontal to the left as the x positive direction, the shape of the BTE can be controlled by adjusting the x coordinates of P_0 , P_1 , P_3 , and P_4 . By making $P_{1x} = P_{3x} = P_{4x} = 0$ and gradually increasing the P_{0x} , M1, M2, M3, and M4 are obtained, which are called Class I (Figure 1b); by gradually increasing the P_{4x} of M4 and keeping the remaining points unchanged, M5, M6, and M7 are obtained, which are called Class II (Figure 1c); by gradually increasing the P_{1x} and P_{3x} of

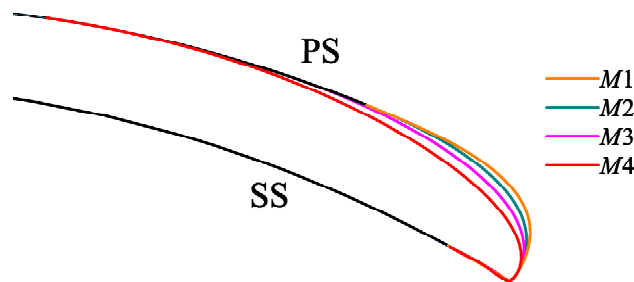
M7 synchronously, with the remaining points unchanged, M8, M9, and M10 are obtained, which are called Class III (Figure 1d); the original model is named M0; the rounding of the trailing edge of the M0 on the PS with different radii lead to M11 and M12, which are classified as Class IV (Figure 1e); and cutting the trailing edge of the M0 on the SS with different angles give us M13, M14, and M15, which are called Class V (Figure 1f). The parameters of all BTE models are shown in Tables 2 and 3.

$$B(t) = \sum_{i=0}^4 \binom{4}{i} P_i (1-t)^{4-i} t^i \tag{1}$$

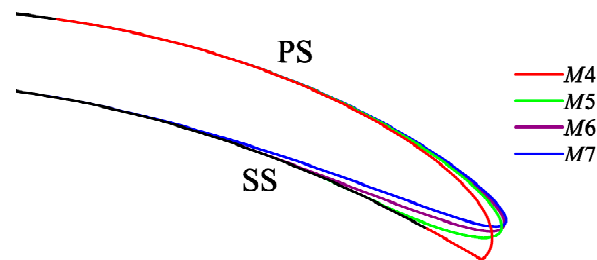
$$= (1-t)^4 P_0 + 4t(1-t)^3 P_1 + 6t^2(1-t)^2 P_2 + 4t^3(1-t) P_3 + t^4 P_4, t \in [0, 1]$$



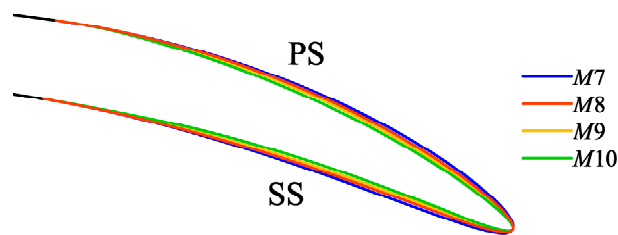
(a) 4th order Bezier curve at the trailing edge



(b) Class I



(c) Class II



(d) Class III

Figure 1. Cont.

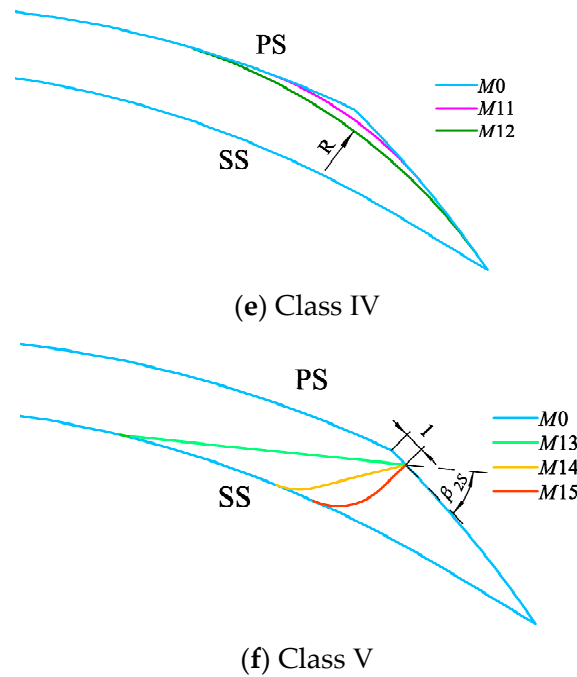


Figure 1. Shapes of different BTE models.

Table 2. Parameters of the Bezier BTE.

M	P _{0x} (mm)	P _{1x} (mm)	P _{3x} (mm)	P _{4x} (mm)
1	6	0	0	0
2	8	0	0	0
3	12	0	0	0
4	20	0	0	0
5	20	0	0	6
6	20	0	0	12
7	20	0	0	20
8	20	6	6	20
9	20	12	12	20
10	20	20	20	20

Table 3. Parameters of the rounded PS and cut SS of the BTE.

M	Description
0	Original BTE
11	R = 20 mm
12	R = 30 mm
13	$\beta_{2s} = 40^\circ$
14	$\beta_{2s} = 60^\circ$
15	$\beta_{2s} = 90^\circ$

3. Numerical Simulation Setup

3.1. Computational Domain and Meshing

As shown in Figure 2, the computational domain of the centrifugal pump consists of five parts: the inlet chamber, impeller, cavity, diffuser, and outlet chamber; furthermore, the full flow field is simulated by considering the leakage of the wear ring and the friction loss of the disc. In order to improve the computational accuracy and efficiency, structure grids are applied to spatially discretize all the computational domains, where the impeller and diffuser are meshed by Turbogrid, and the rest of the domains are meshed by ANSYS ICEM CFD 19R3. The grids near the wall are refined to better capture the boundary layer flow due

to the high-velocity gradient at the wall [17]. The mesh details of the main computational domains are shown in Figure 3. To meet the requirements of the turbulence model for the boundary layer mesh, the average y^+ of all walls of the M0 at the rated flow rate is 5.7, where the average y^+ of the impeller is 11. The y^+ distribution on the M0 blades at the rated flow rate is shown in Figure 4 [28].

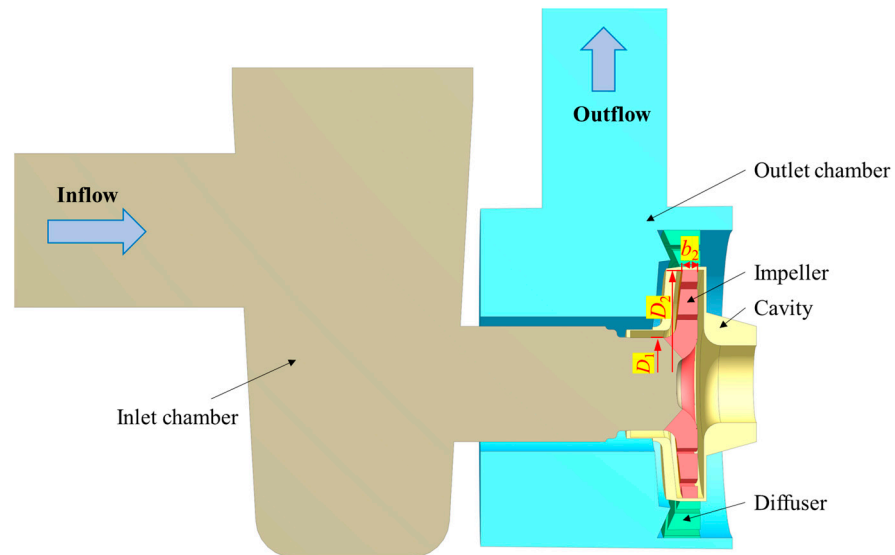


Figure 2. Computational domains of the centrifugal pump.

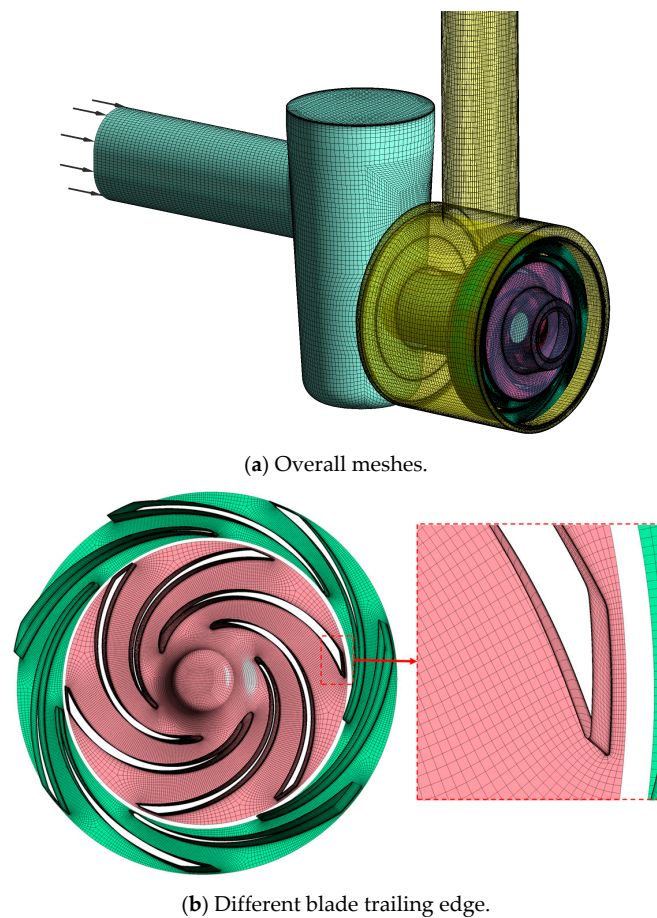


Figure 3. Meshes of the centrifugal pump and blade trailing edge.

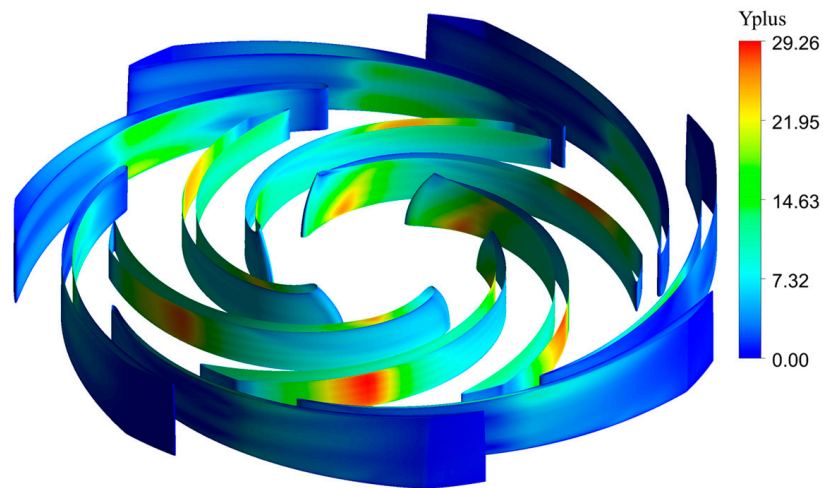


Figure 4. Distribution of y^+ on the blades of the impeller and diffuser on the M0.

The number of grids has an important effect on the results of the simulation. For grid sensitivity analysis, the leakage flows q for different grid numbers are shown in Figure 5. Moreover, the grid convergence indexes (GCI) of the head H , power P , and leakage flow rate q are calculated based on Richardson extrapolation [29] by choosing three grid numbers. The calculation procedure and the meaning of the symbols are shown in [30], and the results are shown in Table 4. Finally, the grid setting of $N_2 = 4.8 \times 10^6$ is selected for subsequent simulations.

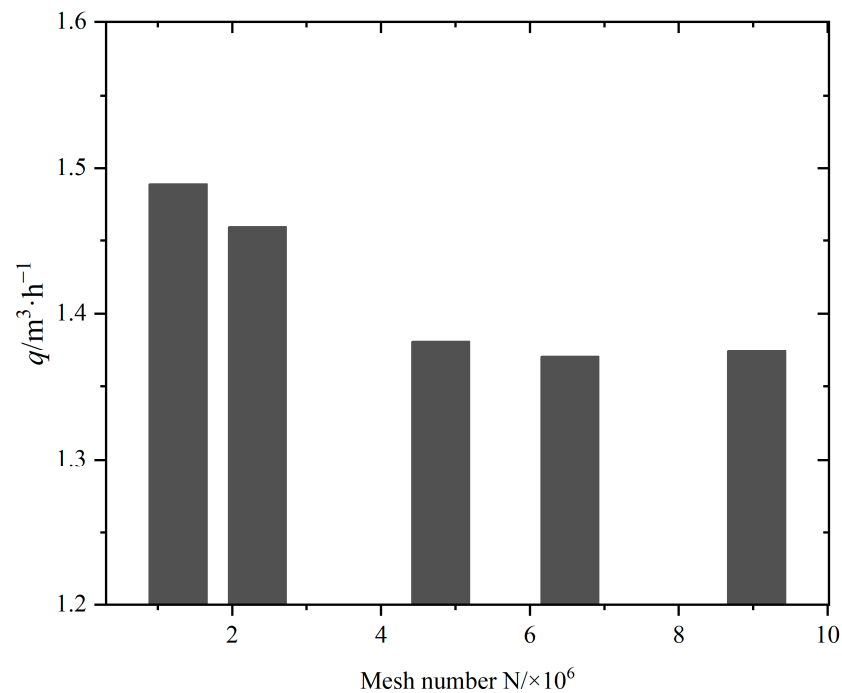


Figure 5. Grid sensitivity analysis.

3.2. Boundary Conditions

The commercial CFD software ANSYS-CFX 19R3 is used to solve the continuity, momentum, and turbulence equations to obtain the performance and internal flow field of the centrifugal pump with different BTEs. The inlet boundary condition is set as a mass flow inlet with a turbulence intensity of 5%. The outlet boundary condition adopts an opening outlet with a relative pressure of 0 Pa. The impeller is set as a rotating domain and the rest are set as a stationary domain. The data transfer between the rotating and stationary

domains is completed by the frozen rotor method. All solid walls are set to no-slip walls with the wall roughness set to smooth walls. The medium is water at 25 °C with a density of 997 kg/m³. The SST $k-\omega$ turbulence model is used to simulate the centrifugal pump with automatic wall function because it can accurately predict the complex flow with separation caused by a high inverse pressure gradient [31–33]. The convection term is solved with high resolution. The root-mean-square residual in the convergence criteria is set to 10⁻⁵.

Table 4. Sample calculations of the discretization error.

	$\Phi = H(\text{m})$	$\Phi = P(\text{W})$	$\Phi = q(\text{m}^3/\text{h})$
$N_1 (\times 10^6)$	9.05	9.05	9.05
$N_2 (\times 10^6)$	4.80	4.80	4.80
$N_3 (\times 10^6)$	2.34	2.34	2.34
r_{21}	1.23	1.23	1.23
r_{32}	1.27	1.27	1.27
Φ_1	14.28	770.55	1.37
Φ_2	14.35	770.85	1.38
Φ_3	14.40	778.31	1.46
p	2.63	13.36	9.97
Φ_{ext}^{21}	14.176	770.530	1.373
e_a^{21}	0.52%	0.039%	0.51%
e_{ext}^{21}	0.71%	0.0025%	0.071%
GCI_{fine}^{21}	0.88%	0.0031%	0.089%
GCI^{23}	0.5%	0.05%	0.72%

4. Results and Discussion

4.1. Experimental Setup and Validation

The impellers of the M0 and M12 are 3D printed and assembled in the centrifugal pump as shown in Figure 6. The experiments are conducted on a closed test rig which consists of an electric centrifugal pump, an electromagnetic flowmeter, two pressure sensors, two valves, a water tank, and pipes as shown in Figure 7. The test facility satisfies the second grade of the international standard ISO 9906:2012(E), and the experiments are conducted under its guidance [34]. The centrifugal pump is driven by a variable frequency motor which is set to a constant speed of 2850 rpm in the experiment; the flow rate is measured by an electromagnetic flowmeter, the inlet pressure and outlet pressure are measured by inlet and outlet pressure sensors, respectively, and the flow rate is regulated by an outlet valve. The information on the experimental instruments is shown in Table 5.

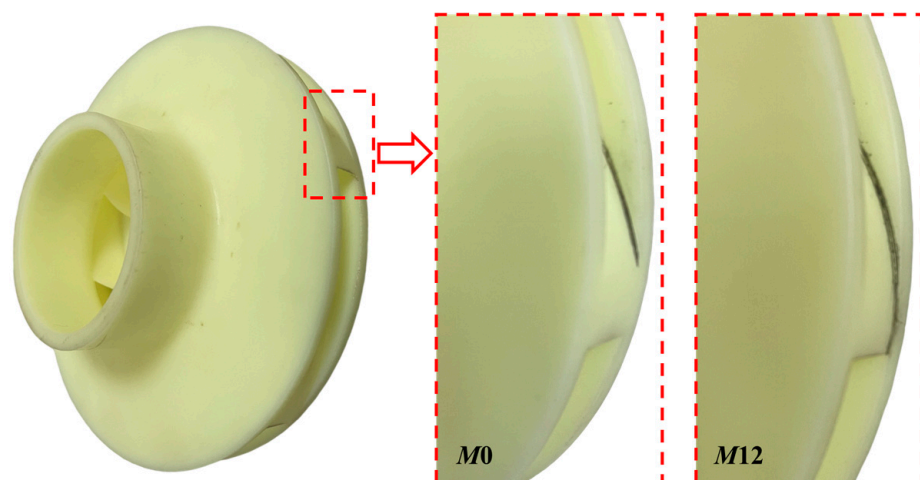


Figure 6. The 3D-printed impellers for M0 and M12.

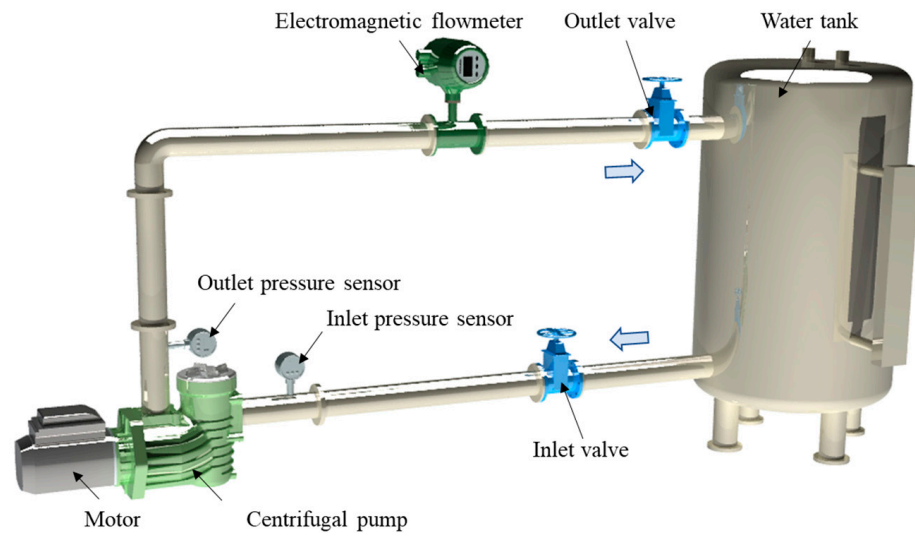
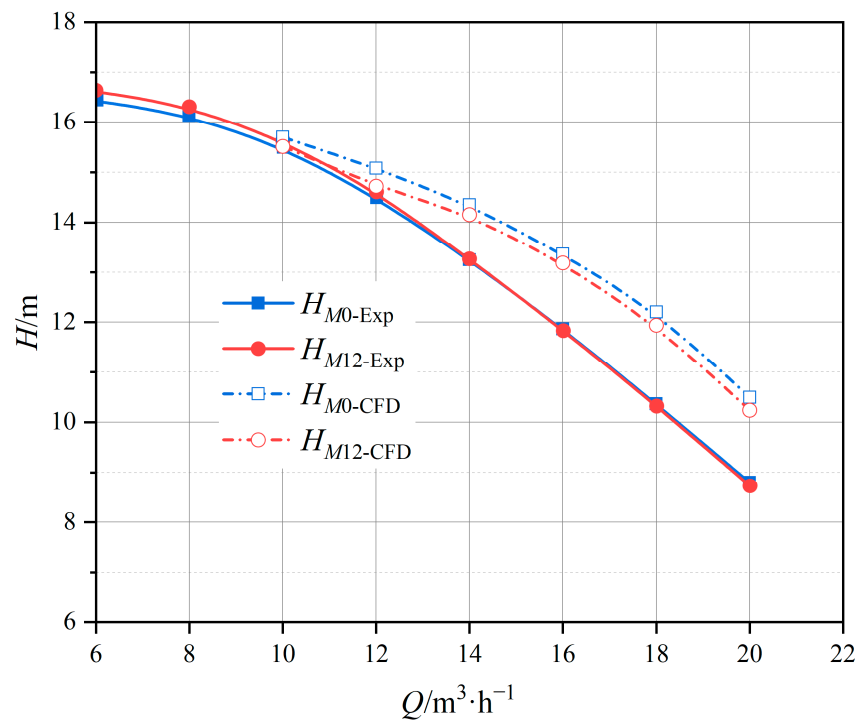


Figure 7. Schematic diagram of the test rig.

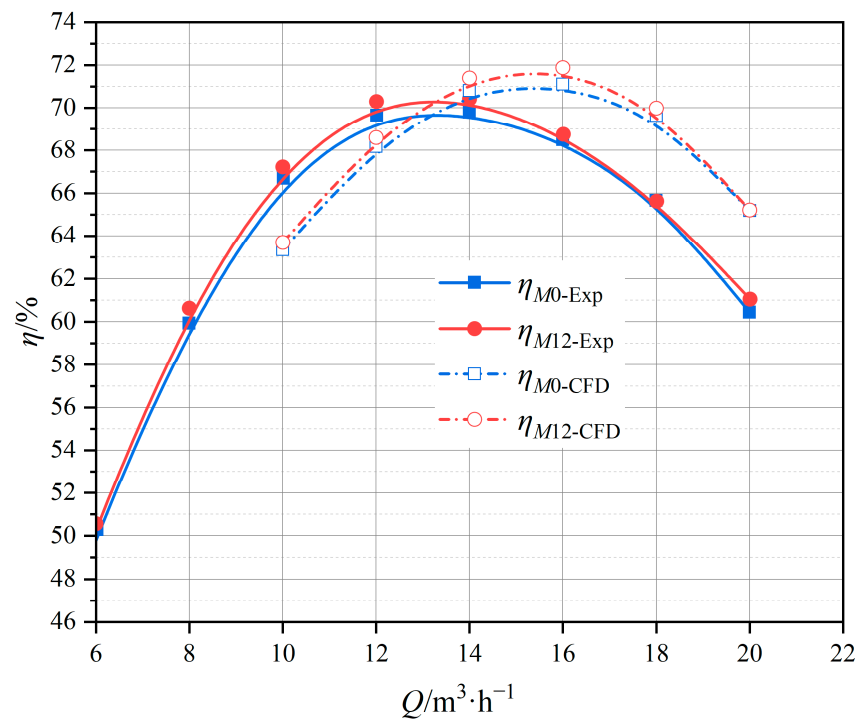
Table 5. Information on the instruments used in the experiment.

Instrument	Sensor Type	Range	Accuracy	Manufacturer
Electromagnetic flowmeter	KEFC DN50 D30000010010160	3.5~35 m ³ /h	±0.5%	Shanghai Kent Instrument Co., Ltd.
Inlet pressure sensor	WT3000TG- 6S22D1B15CM3	−100~100 KPa	±0.075%	Shanghai Welltech Instrument Co., Ltd.
Outlet pressure sensor	WT3000TG- 7S22D1B15CM3	0~1 MPa	±0.075%	Shanghai Welltech Instrument Co., Ltd.

Figure 8a shows the comparison of the simulated and experimental heads of M0 and M12. It can be seen that the experimental head of M12 is higher than M0 at a low flow rate, but slightly lower than M0 at a high flow rate, while the simulated head of M12 is always lower than M0. The simulated and experimental heads are closest around 10 m³/h. As the flow rate increases, the deviation increases, and at the rated point of 14 m³/h, the relative errors between the simulation and experiment of M0 and M12 are 7.6% and 6.2%, respectively. This may be because the BTE angle on the PS of M12 is smaller than that of M0, which increases the absolute flow angle at the impeller trailing edge according to the velocity triangle. Therefore, at low flow rates, the positive attack angle at the diffuser leading edge can be reduced, reducing the impact loss, and thus increasing the head. Whereas at high flow rates, the negative attack angle at the diffuser leading edge is increased, increasing the impact losses, and thus reducing the head. The result of the simulation does not reach this conclusion, probably due to the increase in calculation error when deviating from the rated flow rate. Figure 8b shows the comparison of the simulated and experimental efficiencies of M0 and M12. Compared with M0, the simulated efficiency of M12 is improved, and so is the corresponding experimental efficiency. The simulated and experimental efficiencies show the same trend, with the efficiency of M12 at the rated flow rate improved by 0.59% and 0.63% as compared to that of M0 in the simulation and experiment, respectively. Because over-filing on the PS narrows the wake flowing off the trailing edge, flow losses are reduced and thus efficiency is increased [5]. The optimal efficiency point of the simulation is at 16 m³/h, while that of the experiment is at 14 m³/h. The deviation between the simulation and experiment is minimized at the rated point of 14 m³/h, with relative errors of 1.5% and 1.4% for M0 and M12, respectively. The comparison between the simulation and experiment shows that the simulation results are reliable.



(a) Q-H curves.



(b) Q-η curves.

Figure 8. Comparison of the head and efficiency between the experimental and numerical results of M0 and M12.

4.2. Effect of Different BTEs on Pump Efficiency and the Flow Pattern at Impeller Outlet

For the radial impeller and diffuser, the mainstream flows from the inlet to the outlet along the radial direction. When there is a vortex on the axial plane or meridional section, there is always a part of the fluid that flows opposite to the mainstream direction, which is called a reverse flow. The magnitude of the reverse flow can reflect the chaos and energy

loss of the flow to some extent. The main flow Q and reverse flow Q_{rev} through the flow section S can be calculated as follows [32]:

$$Q = \int_S v_n dS \tag{2}$$

$$Q_{rev} = \int_S \frac{|v_n| - v_n}{2} dS \tag{3}$$

where v_n is the magnitude of the normal velocity component on the flow section S , which is positive when the flow direction is from inward to outward and negative when vice versa.

Since the modification of the BTE is near the impeller trailing edge, as shown in Figure 9, the influence of modifying the BTE on the flow pattern is analyzed by studying the mainstream ratio Q_{ratio} and the uniformity of velocity distribution V_{uni} [35] on the impeller outlet, which is calculated from Equations (4) and (5), respectively.

$$Q_{ratio} = \frac{Q}{Q + Q_{rev}} \times 100\% \tag{4}$$

$$V_{uni} = \left[1 - \frac{1}{\bar{v}} \sqrt{\frac{\sum_{i=1}^n (v_i - \bar{v})^2}{n}} \right] \times 100\% \tag{5}$$

where n is the number of grid nodes on the impeller outlet surface, v_i is the absolute velocity of the i th node, and \bar{v} is the average absolute velocity.

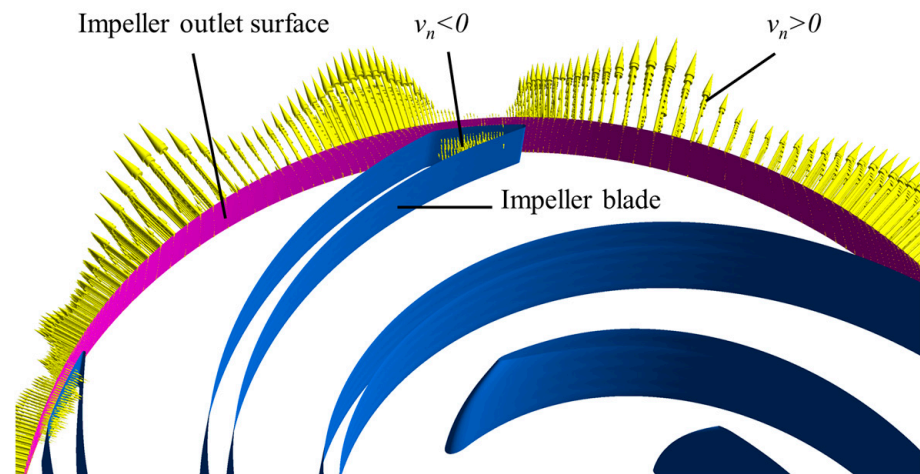


Figure 9. The normal velocity component on the impeller outlet surface.

The effect of different BTEs on the main flow ratio Q_{ratio} , velocity uniformity V_{uni} , and pump efficiency η is shown in Figure 10. It can be seen that in Bezier BTE, η increases from M1 to M10 as the thickness of the BTE decreases, with the largest increase in efficiency in Class I. Q_{ratio} has a similar trend to η . V_{uni} increases gradually from M1 to M3, which is consistent with the variation of η , however, it decreases successively from M3 to M5, which is contrary to the variation of η , and from M5 to M10, V_{uni} is almost unchanged. In Class IV, η , Q_{ratio} , and V_{uni} increase as the radius of the round on the PS of the BTE increases. In Class V, as the cutting angle on the SS of the BTE increases, the BTE gradually becomes blunter, η and Q_{ratio} gradually decrease, while V_{uni} gradually increases. It can be concluded that the reverse flow Q_{rev} can better reflect the variation of pump efficiency η than the velocity uniformity V_{uni} , i.e., the lower the reverse flow of the impeller outlet, the higher the pump efficiency.

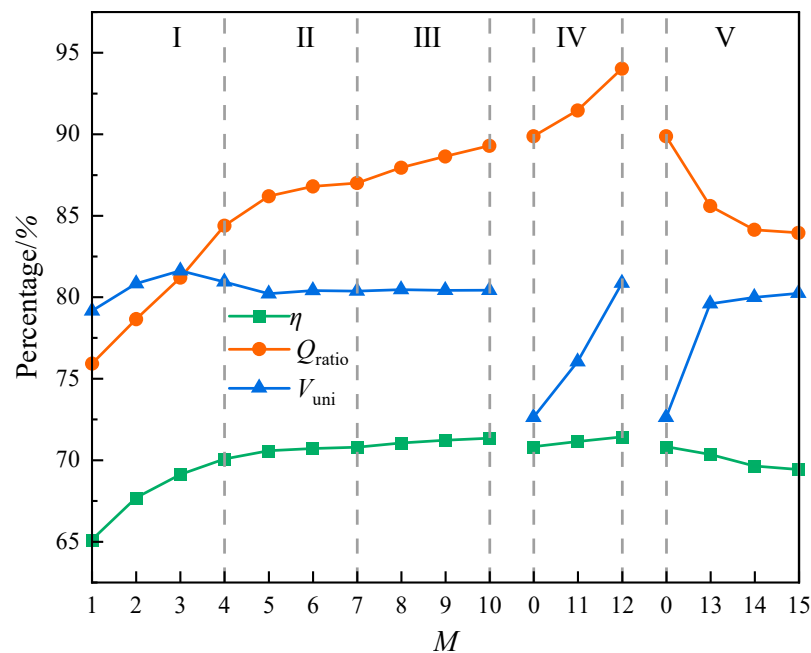


Figure 10. Comparison of pump efficiency and flow regime on impeller outlet for different BTE models.

4.3. Effect of Different BTEs on the Reverse Flow in the Impeller and Diffuser along the Blade-Aligned Streamwise Direction

To study the effect of different BTEs on the reverse flow in the impeller and diffuser along the streamwise direction, the impeller and diffuser are divided equally into 20 parts along the constant blade aligned streamwise (BA Streamwise) as shown in Figure 11. The BA Streamwise of the impeller and diffuser are 0–1 and 1–2, respectively, with 0.05 BA Streamwise for each part. The BA Streamwise of the leading edge (LE) in the impeller and diffuser are 0.25 and 1.25, respectively, and the BA Streamwise of the trailing edge (TE) in the impeller and diffuser are 0.75 and 1.75, respectively. Figure 11 shows a comparison of the reverse flow along the BA Streamwise in the impeller and diffuser for different BTE models. It can be seen that there is almost no reverse flow in all BTE models before the LE of the impeller (BA Streamwise = 0–0.2), and the reverse flow increases suddenly at the LE of the impeller (BA Streamwise = 0.25). After entering the blade passage, the reverse flow decreases immediately and maintains a low value until the BA Streamwise = 0.65–0.75. The reverse flow increases sharply near the impeller BTE. From the BTE to the impeller outlet, the reverse flow continues to increase. After entering the diffuser, the reverse flow decreases rapidly and reaches a minimum near BA Streamwise = 1.4, after which the reverse flow gradually increases. The influence of different BTEs on the reverse flow is mainly reflected in the impeller outlet and diffuser inlet. The larger the reverse flow at the impeller outlet, the larger the reverse flow at the diffuser inlet, indicating that different BTEs affect not only the flow at the impeller outlet but also the flow at the diffuser inlet. In Class I (Figure 12a), different BTEs have the greatest influence on the reverse flow. From M1 to M4, as the BTE gradually becomes thinner, the reverse flow at the impeller outlet and diffuser inlet gradually decreases, and the slope of reverse flow from impeller TE to the impeller outlet gradually increases. In Class II (Figure 12b), from M4 to M7, the slope of the reverse flow from the impeller TE to the impeller outlet decreases, while it has almost no effect on the rest of the region. Additionally, the change from M4 to M5 is the largest due to the biggest geometry change from M4 to M5. In Class III (Figure 12c), the reverse flow at the impeller outlet and the diffuser inlet decreases in parallel as the BTE becomes thinner from M7 to M10. In Class IV (Figure 12d), with the increase in the round radius on the PS of the BTE, the reverse flow slope from the impeller TE to the impeller outlet decreases gradually and the reverse flow from the diffuser inlet to the diffuser LE

decreases in parallel. In Class V (Figure 12e), with the increase in the cutting angle on the SS of the BTE, the reverse flow at the impeller outlet and diffuser inlet increases.

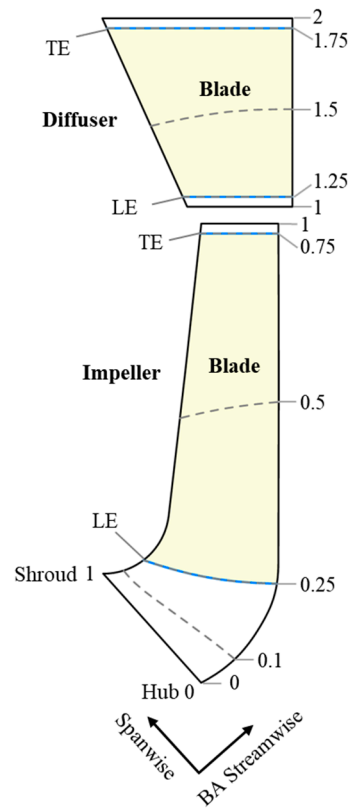
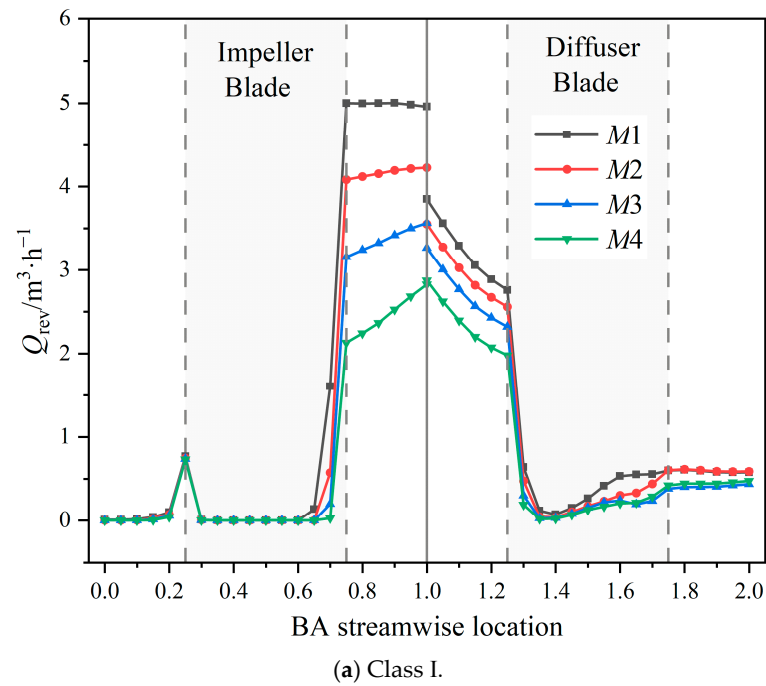
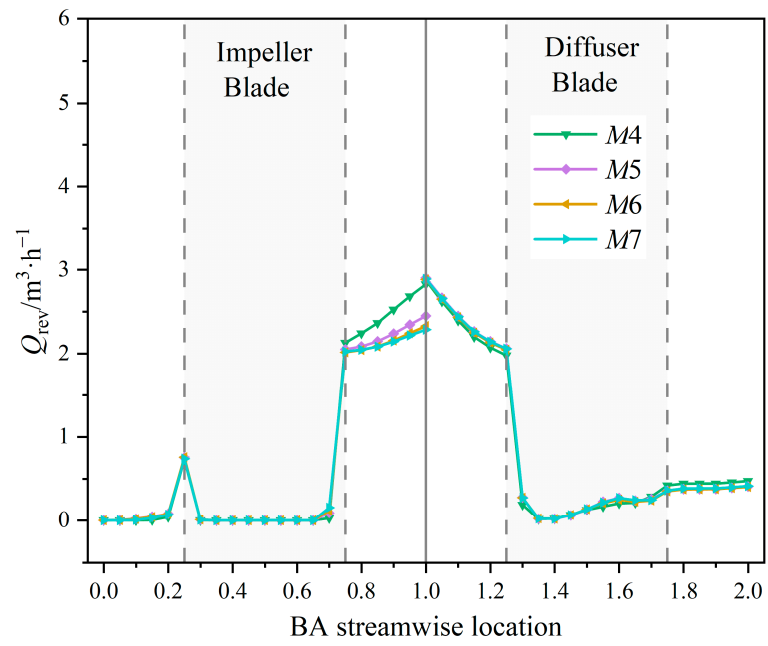


Figure 11. The constant blade aligned streamwise coordinates of the impeller and diffuser.

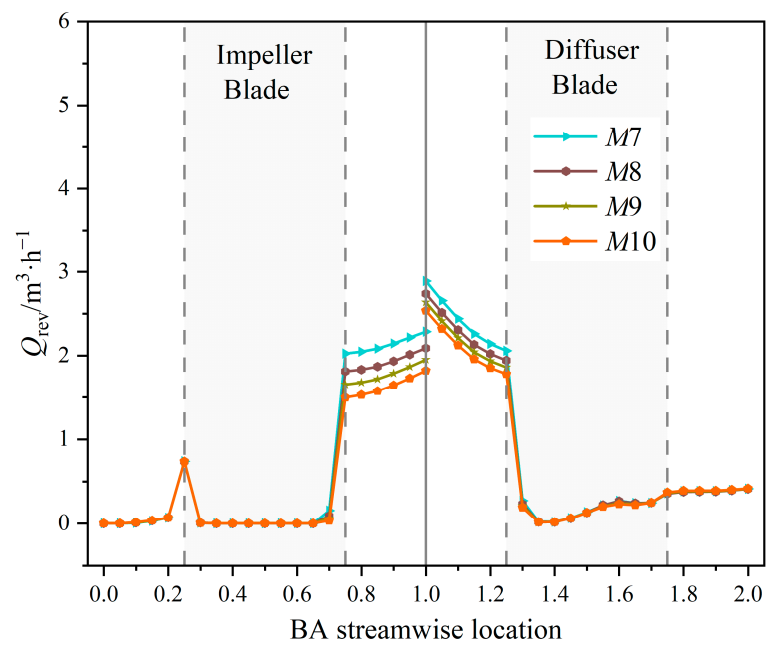


(a) Class I.

Figure 12. Cont.



(b) Class II.



(c) Class III.

Figure 12. Cont.

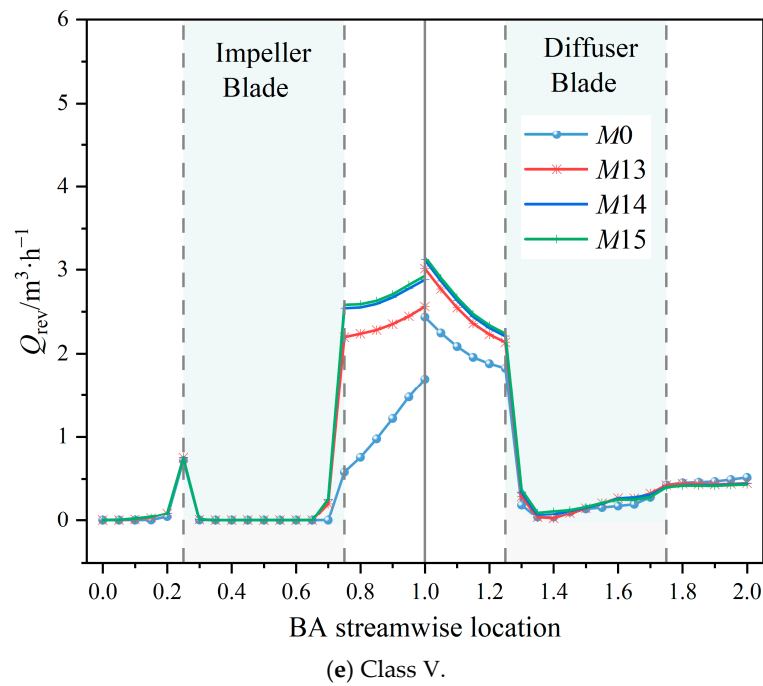
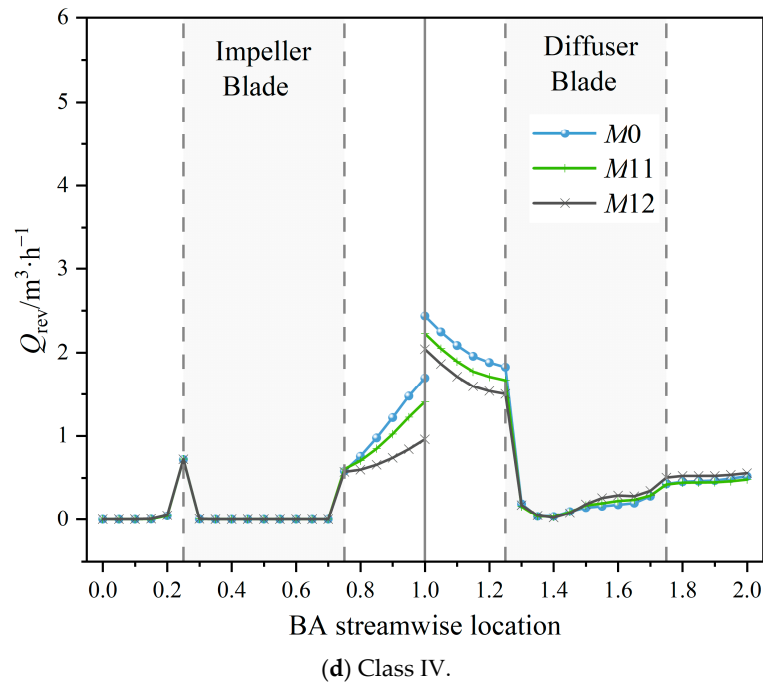
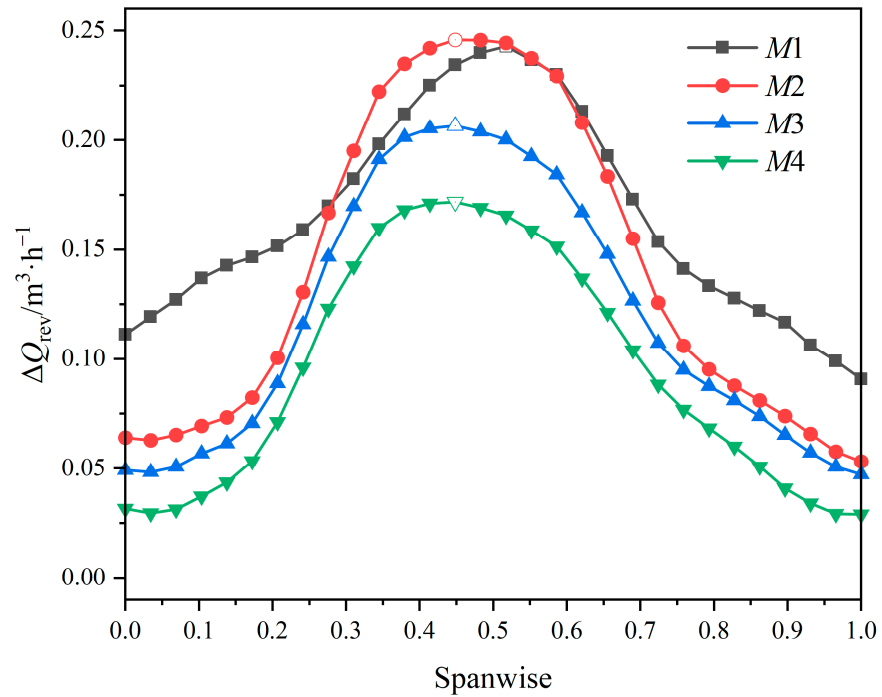


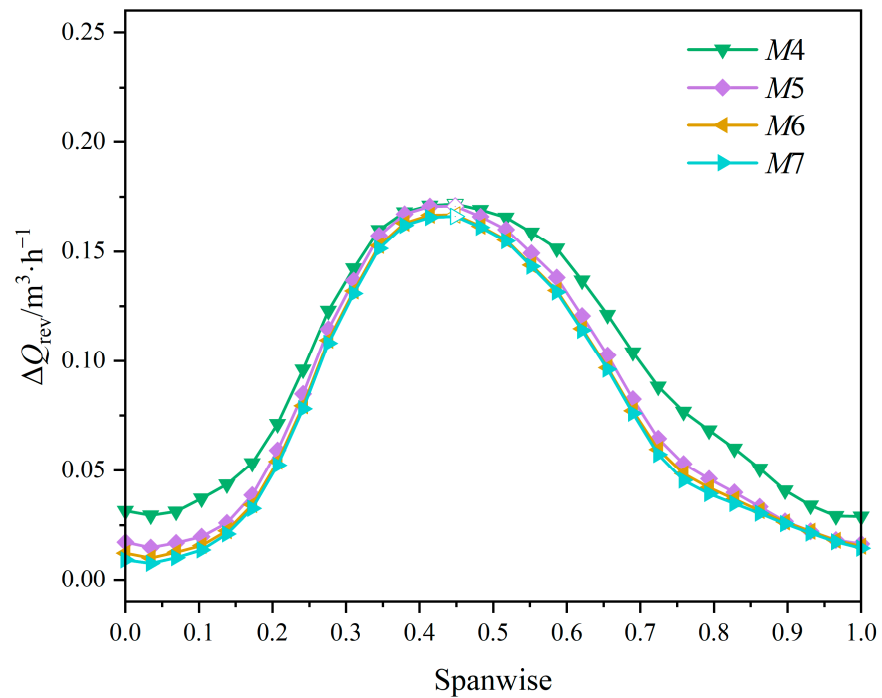
Figure 12. Reverse flow in the impeller and diffuser along the constant BA Streamwise for different BTE models.

We then study the effect of different BTEs on the reverse flow at the impeller outlet along the spanwise direction. A different span represents different blade heights, Span = 0 for the hub and Span = 1 for the shroud. The impeller outlet is divided equally into 30 parts along the spanwise direction, and the reverse flow ΔQ_{rev} of each part is calculated from Equation (3), as shown in Figure 13. It can be seen that the reverse flow at the impeller outlet of different BTE models has similar distribution rules along the spanwise direction, showing a large distribution in the middle and a small distribution on both sides, with a maximum reverse flow near the middle of blade height, which is marked by a hollow symbol. In M1, ΔQ_{rev} reaches its maximum value at Span = 0.52; in M8, M9, M10, M11, and M12, it reaches a maximum value at Span = 0.41; and in the rest of the BTE models,

the maximum value is obtained at Span = 0.45. It can be concluded that the higher the efficiency, the lower the distribution of reverse flow on the impeller outlet and the closer the maximum reverse flow to the hub.

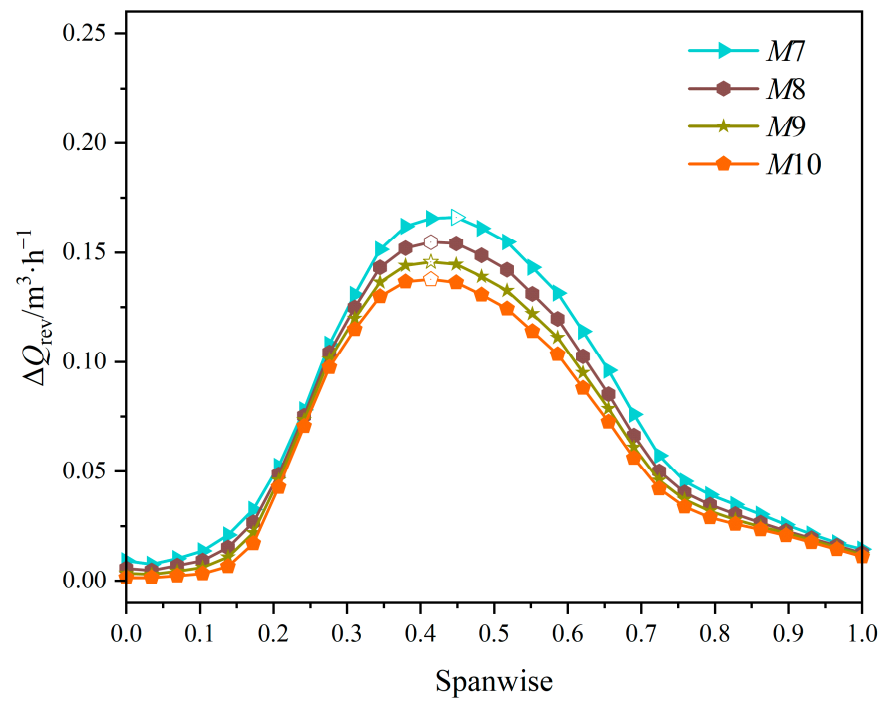


(a) Class I.

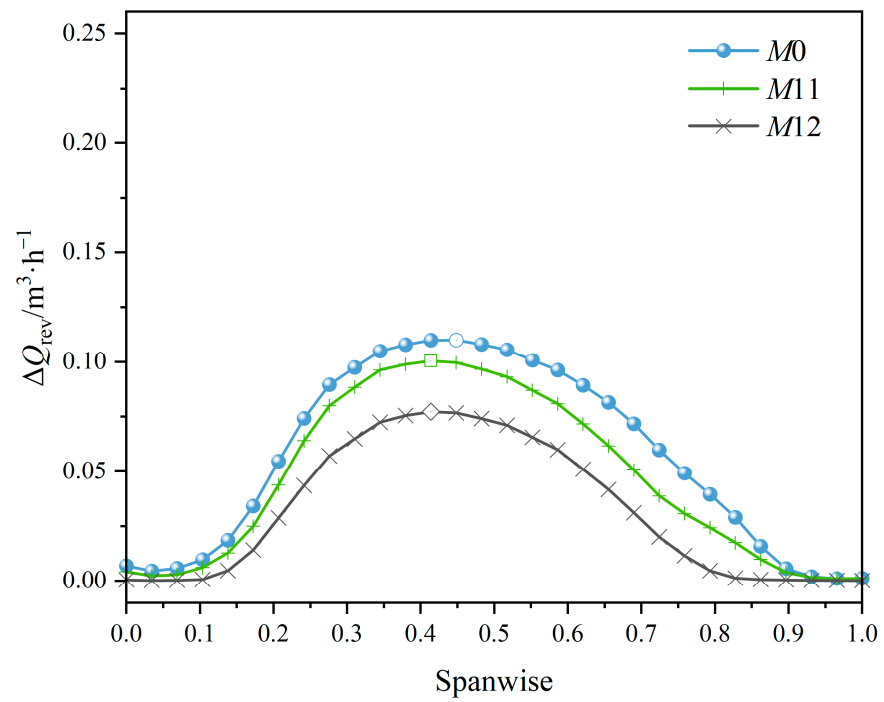


(b) Class II.

Figure 13. Cont.

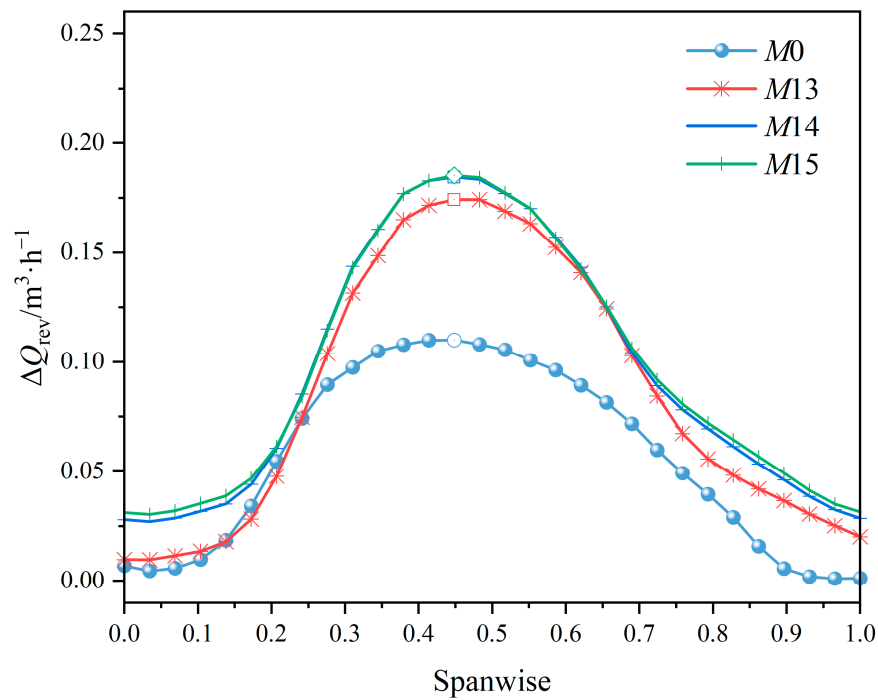


(c) Class III.



(d) Class IV.

Figure 13. Cont.



(e) Class V.

Figure 13. The reverse flow on the impeller outlet along the spanwise direction for different BTE models.

4.4. Effect of Different BTEs on Shaft Power and Energy Loss in the Impeller and Diffuser along the Streamwise Direction

For a closed control body in the fluid domain, without considering gravity, the pressure drop method is used to calculate the energy loss as follows [36]:

$$P_{loss} = T\omega - \iint_A p_i \mathbf{v} \cdot \mathbf{n} dA \tag{6}$$

where T is the torque of the rotating wall on the control body, ω is the rotational speed, the first term on the right is the external power done to the control body, A is the outer surface of the control body, p_i is the total pressure, \mathbf{n} is the outer normal direction of the control body, and the second term on the right is the power increment of the control body.

To study the shaft power and energy loss in the impeller and diffuser at different positions along the streamwise direction, the impeller and diffuser are divided into 20 equal parts along the streamwise direction, Streamwise = 0–1 for the impeller and 1–2 for the diffuser, with each part being 0.05, as shown in Figure 14. Take each part as the control body to calculate its shaft power ΔP and energy loss ΔP_{loss} . Figure 15 shows the distribution of the shaft power ΔP of each control body in the impeller along the streamwise direction for different BTE models. It can be seen that when the Streamwise < 0.15, the shaft power is low, close to 0 W, because there are no blades in this region, and the shaft power is only generated by the shroud and hub due to viscosity. After entering the blade channel, the shaft power gradually rises, forming an inflection point when the Streamwise = 0.25, which is due to the sudden increase in shaft power caused by the impact loss near the impeller LE. After that, the shaft power continues to increase until it reaches the maximum when the Streamwise = 0.7, and then gradually decreases. Different BTE models have little effect on the shaft power in the leading part of the impeller but have a great effect on the shaft power near the impeller trailing edge because the change in the BTE is near the impeller trailing edge. In Class I, due to the large thickness of the BTE, wake vortices caused by flow separation form a large energy loss, so when the Streamwise > 0.9, the shaft power of M1 and M2 increases dramatically. From M1 to M4, the shaft power gradually decreases

near the impeller trailing edge as the BTE becomes thinner. In Class II, since the BTE is thinner than Class I, the energy loss near the impeller outlet is reduced and there is no increase in shaft power along the streamwise direction in M1 and M2. From M4 to M7, the shaft power near the impeller trailing edge gradually increases as the diameter of the BTE increases, with the highest increment from M4 to M5 because of the largest increment of the diameter. In Class III, with the thinning of the BTE, the shaft power near the impeller trailing edge decreases gradually. In Class IV, the shaft power near the impeller outlet of M0 is the highest, and it decreases gradually with the increase in the round radius on the PS of BTE. In Class V, the shaft power near the impeller trailing edge gradually increases with the increase in the cutting angle on the SS of the BTE.

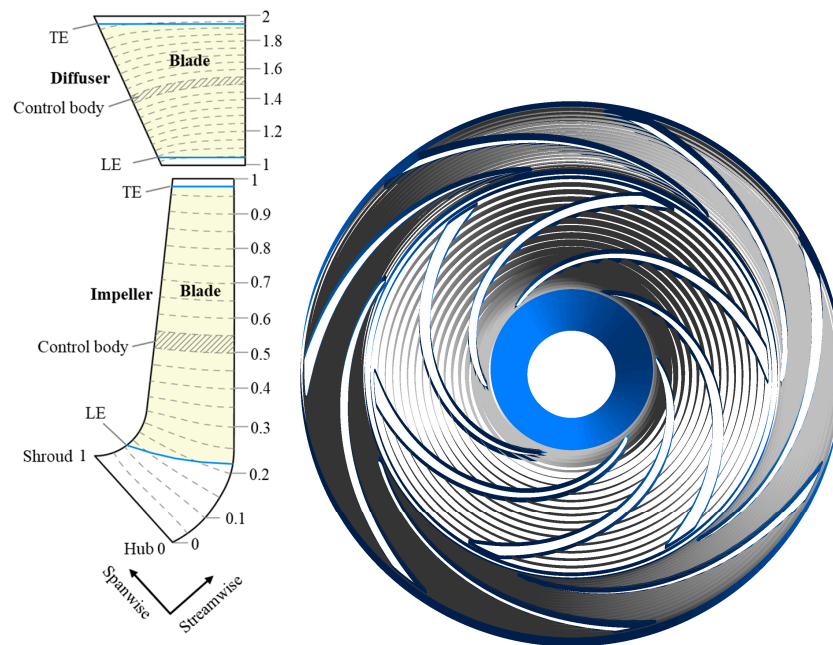


Figure 14. The control bodies of the impeller and diffuser along the constant streamwise location.

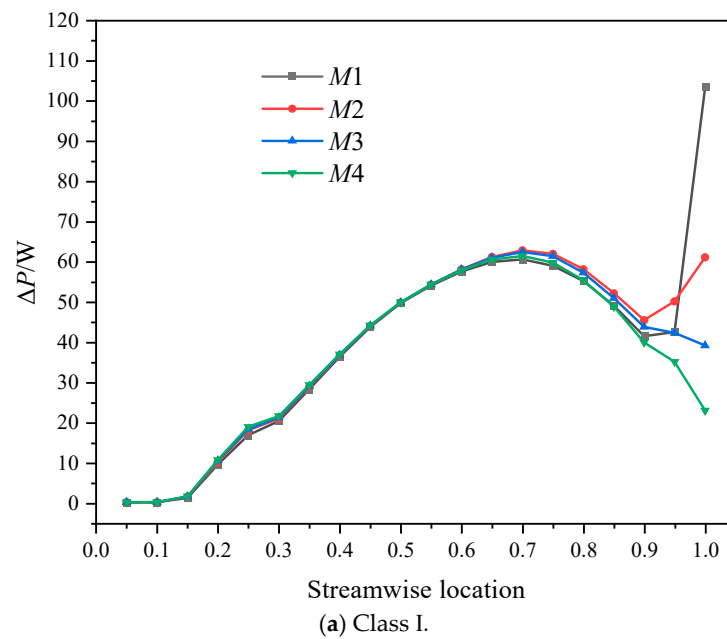


Figure 15. Cont.

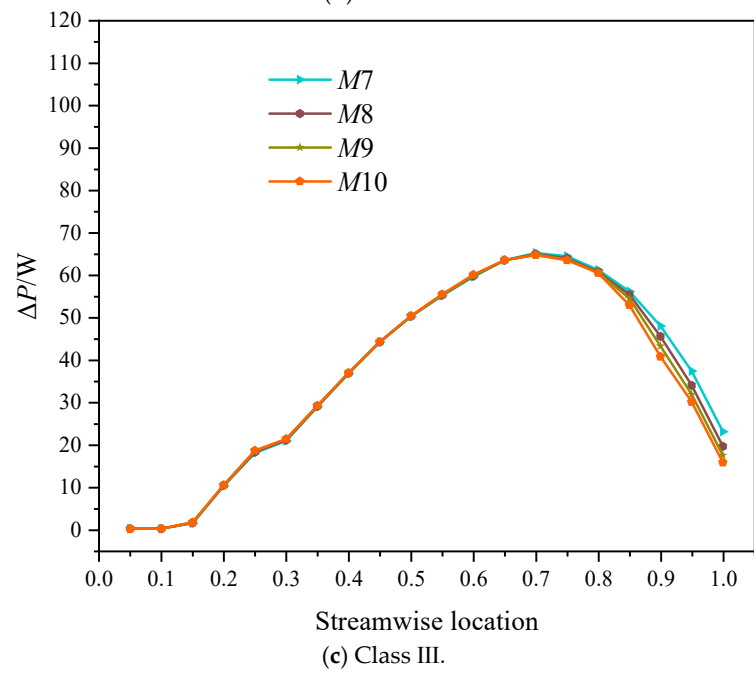
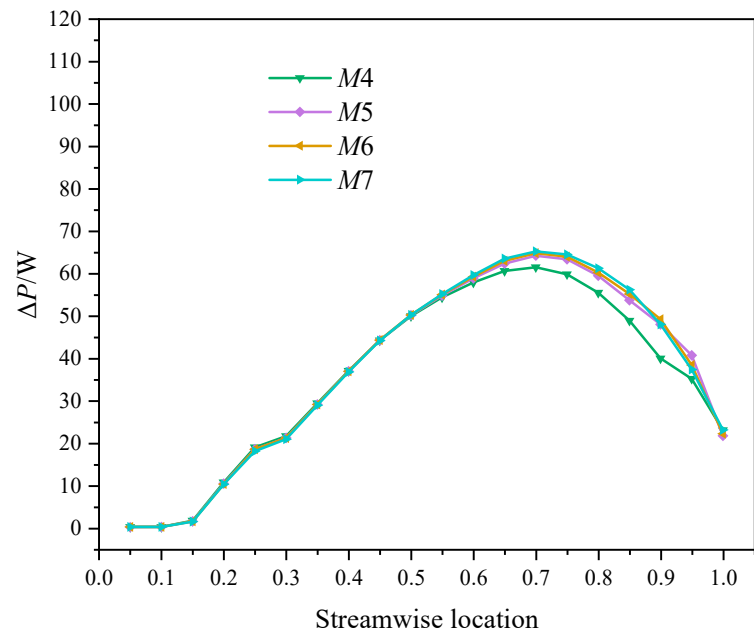
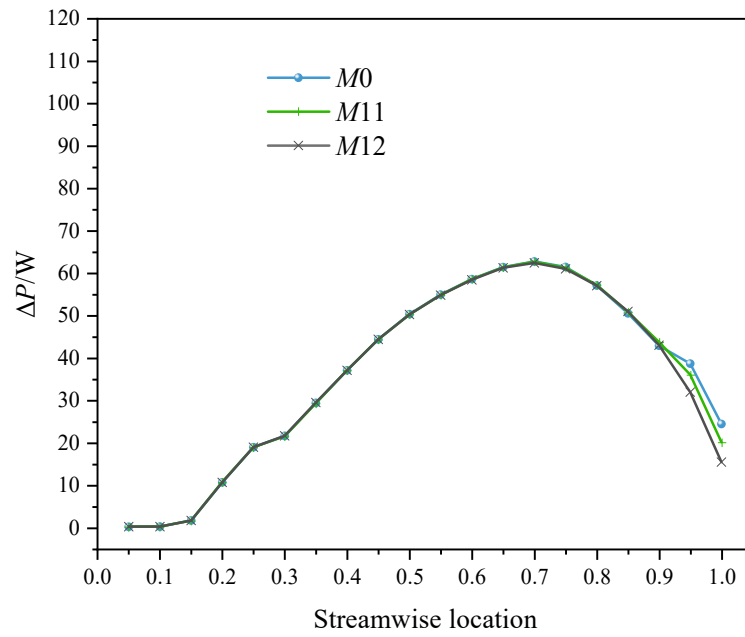
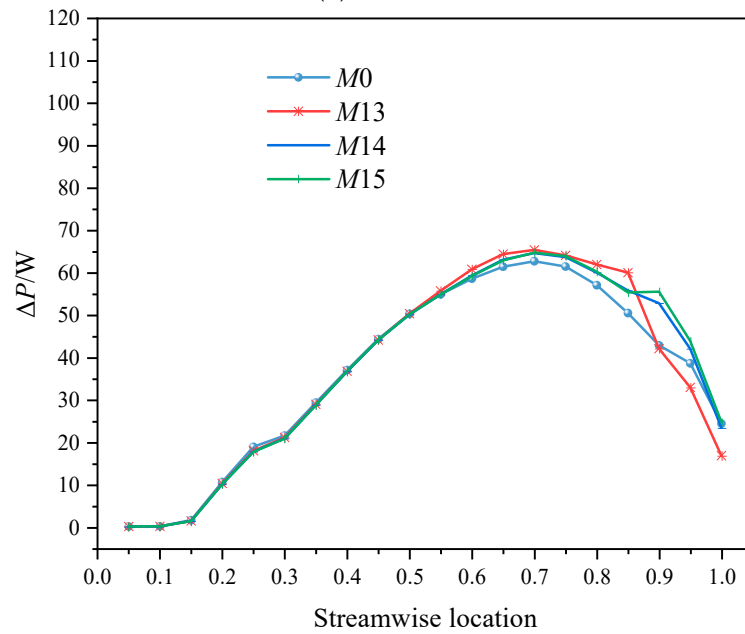


Figure 15. Cont.



(d) Class IV.

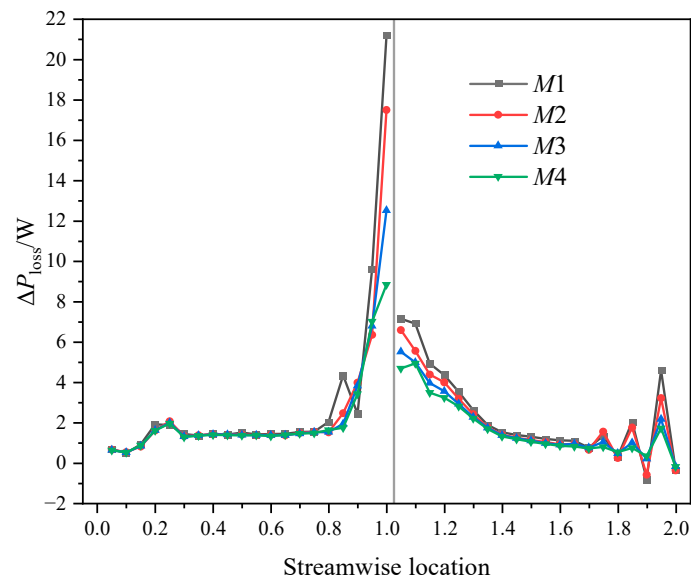


(e) Class V.

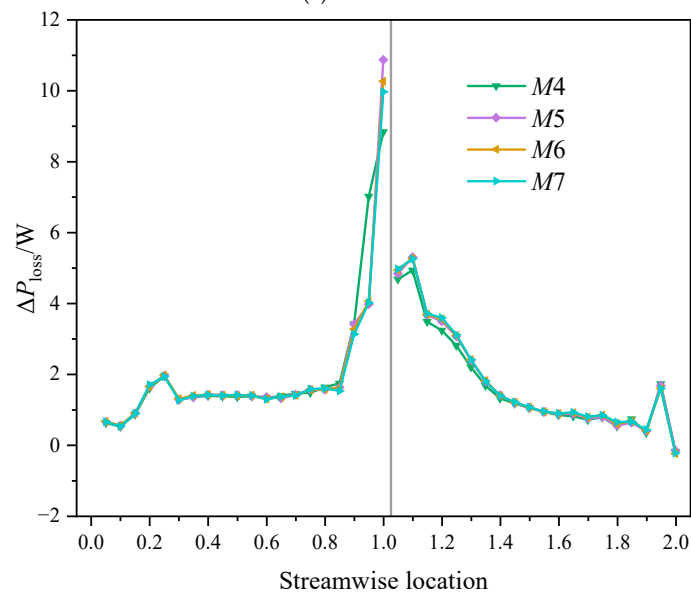
Figure 15. The shaft power of each control body along the streamwise location for different BTE models.

Figure 16 shows the energy loss distribution of each control body in the impeller and diffuser along the streamwise direction for different BTE models calculated by Equation (6). It can be seen that the bladeless region at the inlet of the impeller where Streamwise < 0.15 has a minimum energy loss. The energy loss reaches a local maximum at Streamwise = 0.15~0.25 due to the impact loss. As the Streamwise increases, the energy loss decreases and maintains a low value until the Streamwise = 0.75. When the Streamwise > 0.75, all the BTE models show a dramatic increase due to the influence of the BTE. The energy loss in the diffuser decreases gradually from the inlet to the outlet in general, with the exception of a local maximum at the diffuser TE where the Streamwise = 1.9~1.95, which may be due to the effect of the wake vortex at the diffuser TE. Different BTEs have a great effect not only on the energy loss of the impeller outlet but also on the energy loss of the diffuser inlet while having little effect on the energy loss in the leading part of the impeller where the

Streamwise < 0.75, just like the effect on reverse flow. The influence of the impeller BTE on the energy loss of the diffuser is mainly reflected in the Streamwise region 1~1.4. The energy loss in the diffuser inlet is mainly affected by the energy loss in the impeller outlet; as a whole, the higher the energy loss in the impeller outlet, the higher the energy loss in the diffuser inlet. The energy loss in the bladeless region of the diffuser inlet, where the Streamwise = 1~1.05, is mainly affected by the impeller outlet, where the Streamwise = 0.95~1, and the energy loss at diffuse LE where the Streamwise = 1.05~1.1 is mainly affected by the impact loss of the diffuser blade. It can be found that when the energy loss at the impeller outlet (Streamwise = 0.95~1) is greater than 11.6W, that is, in M0, M1, M2, and M3, the energy loss in the bladeless region (Streamwise = 1~1.05) of the diffuser inlet is greater than that at diffuser LE (Streamwise = 1.05~1.1), while in the rest of the BTE models, the contrary conclusion is reached.

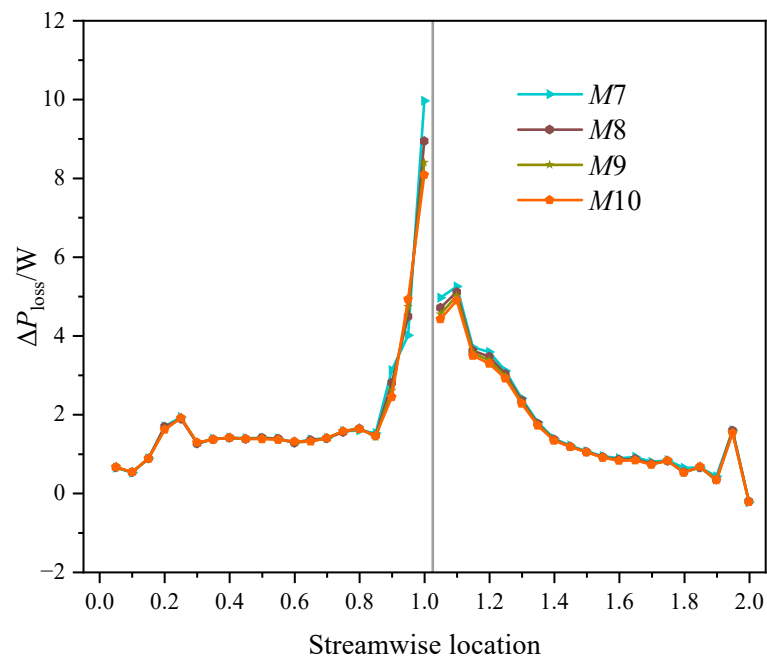


(a) Class I.

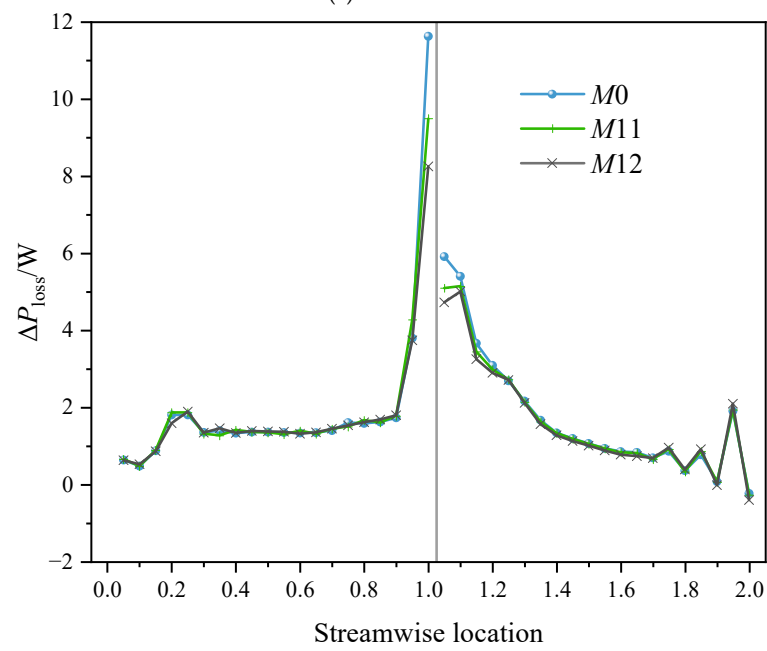


(b) Class II.

Figure 16. Cont.



(c) Class III.



(d) Class IV.

Figure 16. Cont.

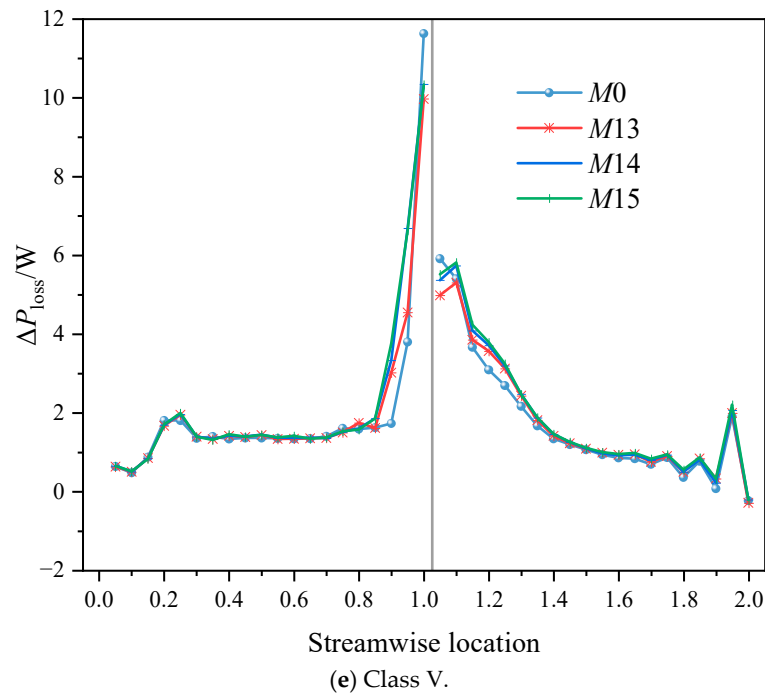


Figure 16. The energy loss of each control body in the impeller and diffuser along the streamwise location for different BTE models.

4.5. Effect of Different BTEs on Entropy Production in the Impeller and Diffuser

In centrifugal pumps, due to the viscosity of the medium [37], in the near-wall region, the shear stresses make it inevitable that some of the kinetic and pressure energy of the fluid is converted into internal energy. In the high Reynolds number region, unstable turbulent pulsation will also inevitably generate energy losses [36]. According to the second law of thermodynamics, these energy losses will result in an increase in entropy. Therefore, the entropy production theory can be used to study the energy loss in a centrifugal pump with different BTEs. The local entropy production rate without considering heat transfer and temperature rise is calculated as follows [38–40]:

$$\dot{S}_{PRO,D} = \dot{S}_{PRO,\bar{D}} + \dot{S}_{PRO,D'} \tag{7}$$

$$\dot{S}_{PRO,\bar{D}} = \frac{\mu}{T} \left\{ 2 \left[\left(\frac{\partial \bar{u}_1}{\partial x_1} \right)^2 + \left(\frac{\partial \bar{u}_2}{\partial x_2} \right)^2 + \left(\frac{\partial \bar{u}_3}{\partial x_3} \right)^2 \right] + \left(\frac{\partial \bar{u}_2}{\partial x_1} + \frac{\partial \bar{u}_1}{\partial x_2} \right)^2 + \left(\frac{\partial \bar{u}_3}{\partial x_1} + \frac{\partial \bar{u}_1}{\partial x_3} \right)^2 + \left(\frac{\partial \bar{u}_2}{\partial x_3} + \frac{\partial \bar{u}_3}{\partial x_2} \right)^2 \right\} \tag{8}$$

$$\dot{S}_{PRO,D'} = \frac{\mu}{T} \left\{ 2 \left[\overline{\left(\frac{\partial u'_1}{\partial x_1} \right)^2} + \overline{\left(\frac{\partial u'_2}{\partial x_2} \right)^2} + \overline{\left(\frac{\partial u'_3}{\partial x_3} \right)^2} \right] + \overline{\left(\frac{\partial u'_2}{\partial x_1} + \frac{\partial u'_1}{\partial x_2} \right)^2} + \overline{\left(\frac{\partial u'_3}{\partial x_1} + \frac{\partial u'_1}{\partial x_3} \right)^2} + \overline{\left(\frac{\partial u'_2}{\partial x_3} + \frac{\partial u'_3}{\partial x_2} \right)^2} \right\} \tag{9}$$

where $\dot{S}_{PRO,\bar{D}}$ is the entropy production rate by direct dissipation and $\dot{S}_{PRO,D'}$ is the entropy production rate by turbulent dissipation.

Since Equation (9) is unclosed, in the case of the finite Reynolds number in the SST *k-ω* turbulence model, $\dot{S}_{PRO,D'}$ can be approximated as [19]:

$$\dot{S}_{PRO,D'} = \beta \frac{\rho \omega k}{T} \tag{10}$$

where $\beta = 0.09$, ω is the turbulent eddy frequency, and k is the turbulence energy.

To analyze the effect of different BTEs on the magnitude and location of energy loss in the impeller and diffuser, the least efficient model, M1, the most efficient models, M10 and M12, and the original model, M0, are selected to analyze the local entropy production rate $\dot{S}_{PRO,D}$ on different Span and impeller outlets. As shown in Figure 17, different BTE models have the greatest effect on the entropy production of the impeller outlet and diffuser inlet but have little effect on the entropy production of the leading part of the impeller. The closer to the shroud, the higher the entropy production is on the SS of the impeller LE, which is due to the increase in relative velocity and impact loss near the shroud. M1 has the largest area of high entropy production, which is located at the SS of the impeller TE and diffuser LE. After thinning the BTE, the entropy production of M10 decreases significantly. After rounding the PS of the BTE, M12, the entropy production lowers slightly compared to that of M0. On the surface of Span = 0.5, influenced by the shape and thickness of the BTE and jet-wake effect [21], strong shear action near the impeller BTE causes wake development and vortex shedding [41], forming a triangular region of high entropy production from the SS to PS near the impeller outlet. The area of the triangle and the angle near the BTE gradually decrease in the order of M1, M10, M0, and M12, indicating that the blunter the BTE is, the greater the entropy production and energy loss will be [42]. On the surface of Span = 0.95, the area of the high entropy production located at the SS of the diffuser LE is affected by the impeller BTE and gradually decreases in the order of M1, M0, M10, and M12.

From the above analysis, it can be seen that the impeller outlet is the area with the largest energy loss and highest entropy production, and also the flow section with the largest reverse flow in the impeller. To investigate the effect of different BTEs on the entropy production and reverse flow of the impeller outlet, the entropy production and velocity vector of the reverse flow of the impeller outlet for M0, M1, M10, and M12 are analyzed, as shown in Figure 18, which is viewed from the inside to the outside to better display the reverse flow. It can be seen that the high entropy production area is located near the SS of the BTE and the reverse flow area is located at the SS of the BTE near the middle span. In general, where the reverse flow is greater, the entropy production is greater. M0, M10, and M12 have high entropy production at Span = 0.2–0.3. The entropy production of M10 and M12 is significantly lower than that of M0 and M1. The entropy production on the impeller outlet $E_{PRO,D}$ is calculated by Equation (11) for quantitative analysis, and the values of $E_{PRO,D}$ in Table 6 show a decreasing order of M1, M0, M10, and M12.

$$E_{PRO,D} = \int_S \dot{S}_{PRO,D} dS \tag{11}$$

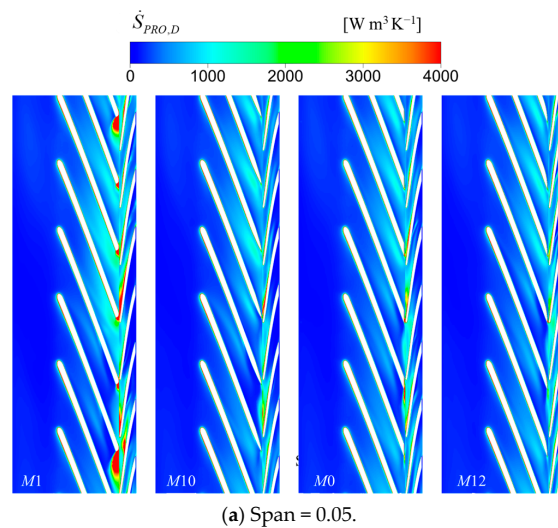


Figure 17. Cont.

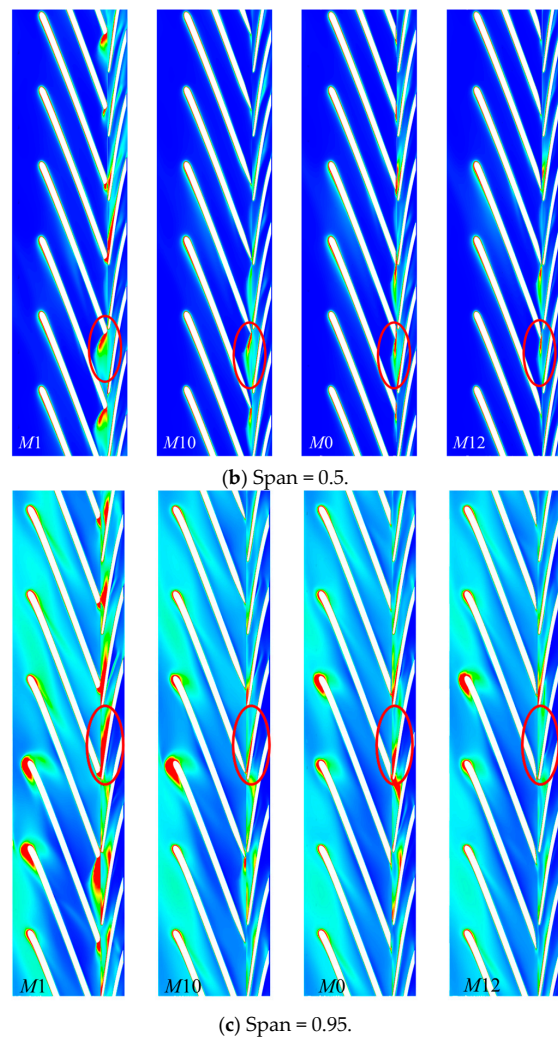


Figure 17. Local entropy production distribution on different Span values in the impeller and diffuser for different BTE models.

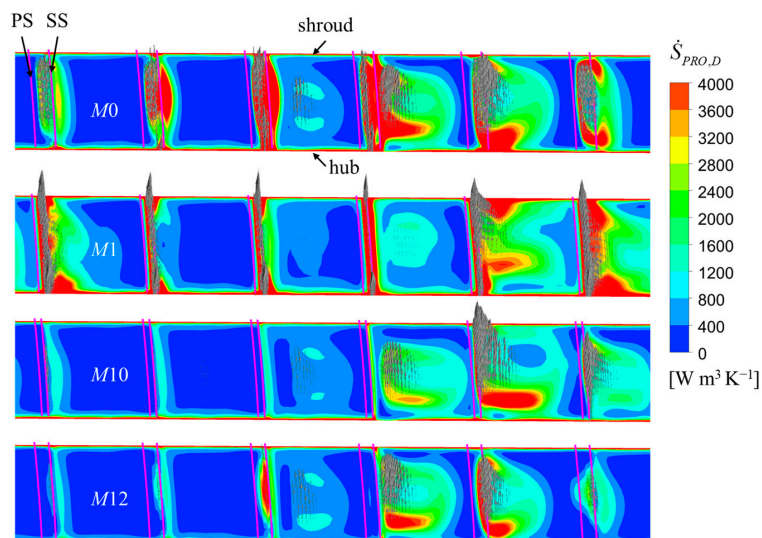


Figure 18. The local entropy production distribution and velocity vector of the reverse flow on the impeller outlet for different BTE models.

Table 6. The entropy production on the impeller outlet for different BTE models.

Model	M0	M1	M10	M12
$E_{PRO,D}$ (W·m ⁻¹ ·K ⁻¹)	5.778	8.446	3.032	2.911

4.6. Effect of Different BTEs on Vortex Structure and Flow Field in the Impeller and Diffuser

To further investigate the effect of different BTEs, the vortex identification method is used to visualize the vortices structure in the impeller and diffuser. Compared with the Q criterion and λ_2 method, the Ω method is less sensitive to the threshold and can identify both weak and strong vortices. Therefore, the Ω -vortex identification method is used to identify vortices in the impeller and diffuser [43,44]. The expressions are as follows:

$$\Omega = \frac{\|\mathbf{B}\|_F^2}{\|\mathbf{A}\|_F^2 + \|\mathbf{B}\|_F^2 + \varepsilon} \tag{12}$$

$$\mathbf{A} = \frac{1}{2}(\nabla v + \nabla v^T) \tag{13}$$

$$\mathbf{B} = \frac{1}{2}(\nabla v - \nabla v^T) \tag{14}$$

$$\varepsilon = 0.001 \times (\|\mathbf{B}\|_F^2 - \|\mathbf{A}\|_F^2)_{max} \tag{15}$$

where $\|\cdot\|_F$ represents the Frobenius norm, \mathbf{A} and \mathbf{B} represent the symmetric and antisymmetric parts of the velocity gradient tensor, respectively, and ε is a small positive number to avoid large errors caused by the zero denominator. The vortex is displayed by an isosurface of $\Omega = 0.52$. Figure 19 shows the vortex structure in the impeller and diffuser for different BTE models. It can be seen that the vortices are located in the impeller LE (region B), impeller TE (region A), and diffuser LE, indicating that the flow in these regions is chaotic, resulting from flow separation and strong vortices caused by the high-velocity gradient. Different BTEs have greater effects on the impeller TE. To analyze the flow at the impeller TE, seven sections (S1–S7) are made in region A along the flow direction to display the swirling strength and velocity vectors, and 3D streamlines are generated along the PS of the impeller blade, as shown in Figure 20. In M1, because it has the thickest BTE, a large area of attached vortices is formed on the PS of the BTE. After leaving the BTE, vortex shedding is formed due to flow separation, resulting in two contra-rotating wake vortices near the shroud and hub. The swirling strength in the vortex core is the largest, and the swirling strength near the shroud is greater than that near the hub. The swirling strength gradually weakens with the increase in the distance from the BTE, and the streamline becomes more chaotic due to the influence of the vortex, leading to a reverse flow along the blade surface near the BTE. The vortex size and swirling strength of M10 are significantly lower than that of M1, and the flow is improved. At the junction of the PS and the BTE in M0, a vortex is formed due to the abrupt change of curvature, but the size and strength of the vortex are slightly reduced compared to that of M10. In M12, generated by rounding off the junction of the PS and the BTE in M0, the vortex here disappears, and the streamline distribution is more uniform than that of M0.

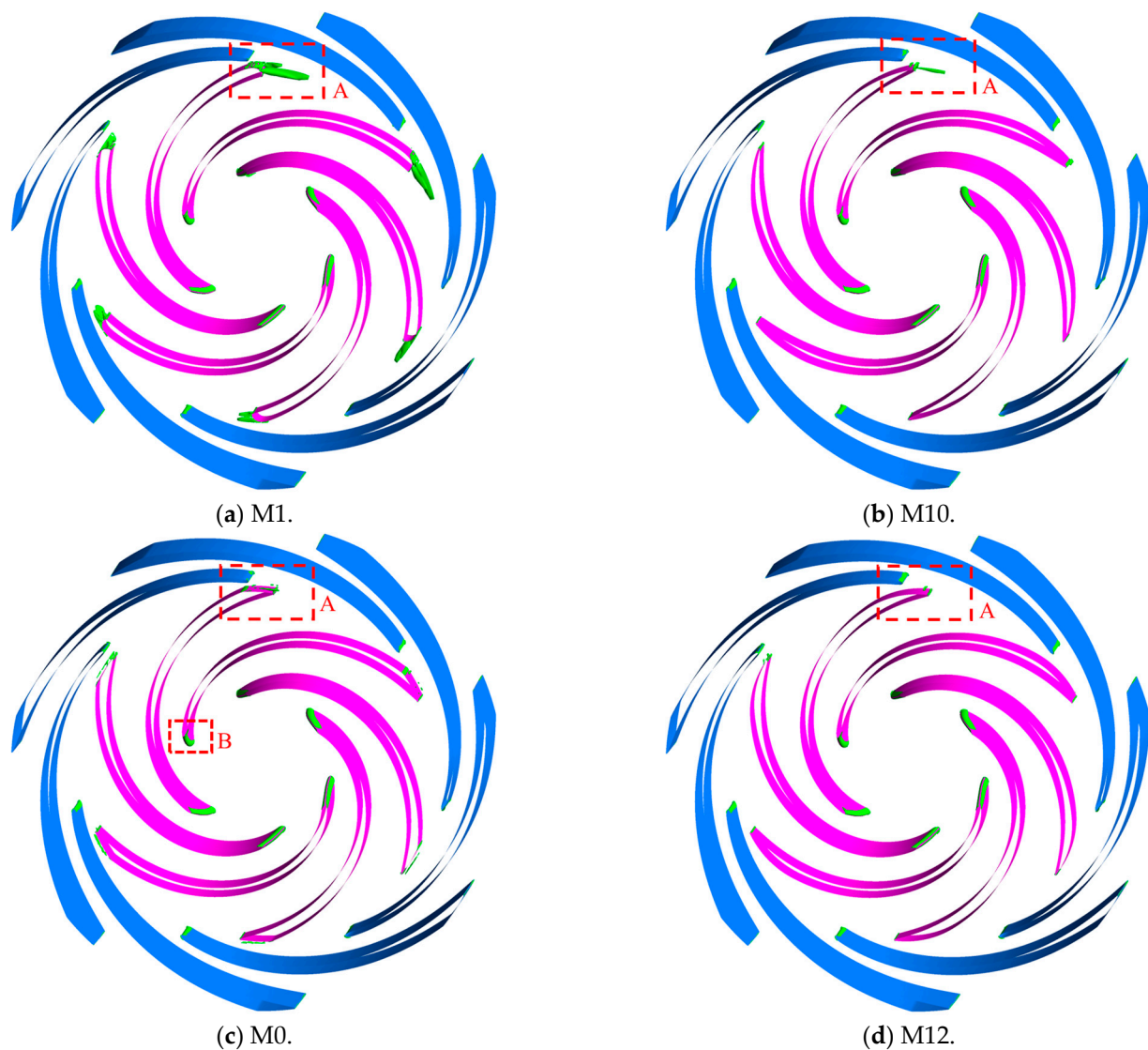


Figure 19. The vortex structure in the impeller and diffuser for different BTE models.

From the above analysis, it can be seen that the energy loss, entropy production, reverse flow, and vortex intensity have a local maximum at the impeller LE, and different BTEs have almost no effect on the flow pattern here. Therefore, only region B in M0 is analyzed. Figure 21 shows the velocity and pressure distribution at the impeller LE on the surface of $\text{Span} = 0.5$ in M0. It can be seen that the fluid facing the blade LE gradually slows down under the blockage of the blade due to its thickness, forming a stagnation point at the LE of the blade (Figure 21a). According to the Bernoulli equation in rotating coordinates [45], the pressure near the stagnation point increases as shown in Figure 21b. Under the pressure difference, the fluid near the stagnation point flows along the blade surface in opposite directions to both sides, thus creating a reverse flow at the impeller LE. With the action of a positive pressure gradient and centrifugal force, the fluid velocity on both sides of the stagnation point increases rapidly, forming a higher velocity gradient, so a higher vortex intensity and energy loss are formed on both sides of the stagnation point. Influenced by the axial vortex resulting from the rotation of the impeller, the velocity at the SS of the LE is higher than that at the PS of the LE, forming a local high-speed and low-pressure area at the SS of the LE.

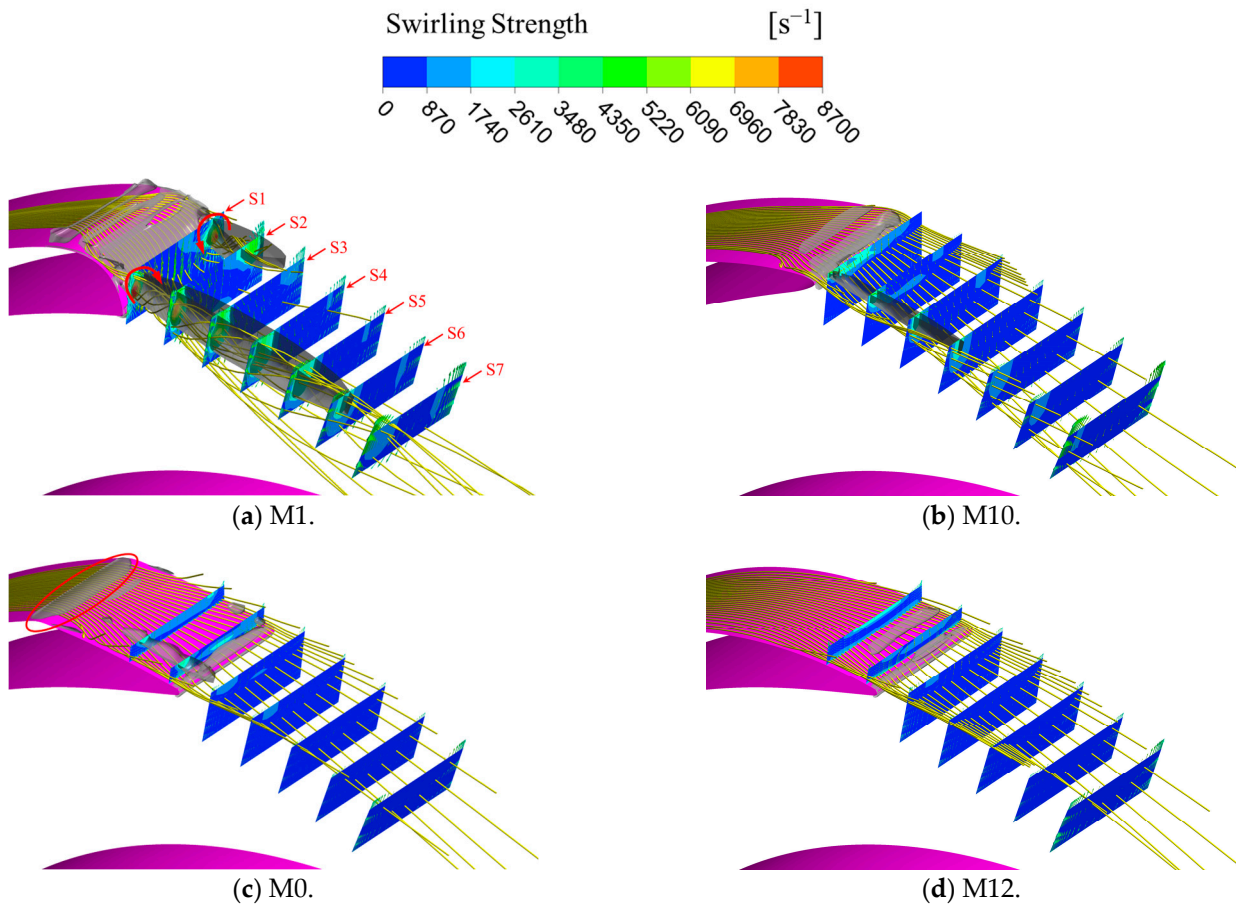


Figure 20. Distribution of the swirling strength, velocity vector, and streamline at the impeller outlet for different BTE models.

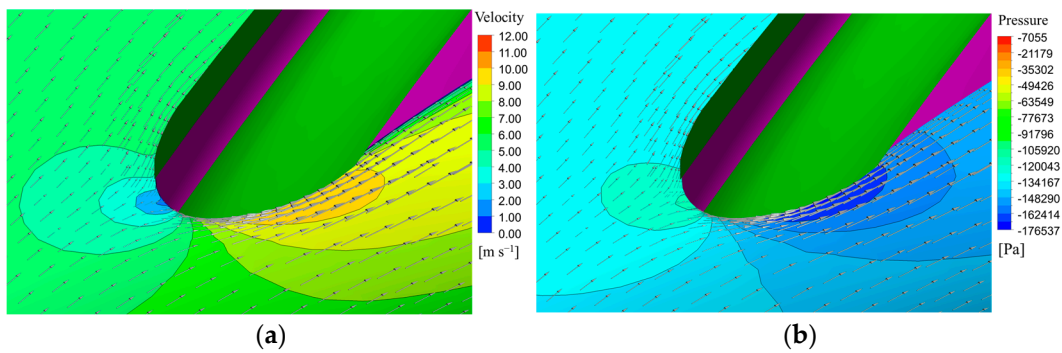


Figure 21. Velocity and pressure distribution at the leading edge of the impeller on the surface of Span = 0.5 in M0. (a) Velocity contour and velocity vector and (b) pressure contour and velocity vector.

4.7. Effect of Different BTEs on the Stress and Deformation of Impeller

A change in the shape of the BTE will result in a change in the blade thickness, which may affect the strength of the impeller. Obviously, the shape of the blade must ensure that its mechanical strength is not jeopardized [5]. To accurately calculate the impeller stress and deformation, a one-way fluid-structure interaction analysis is carried out in the Static Structural module of the Ansys Workbench. The solid impeller is meshed as shown in Figure 22, then fixed support is applied to the shaft end, the rotational velocity of the impeller is set as 2850 rpm, and the pressure is calculated by CFX and is loaded onto the impeller surface. Equivalent stress and total deformation are calculated using

finite element analysis and the fourth strength theory [46]. The material of the impeller is PA66 with density $\rho = 1140 \text{ kg/m}^3$, elastic modulus $E = 1.48 \text{ GPa}$, Poisson's ratio $\mu = 0.41$, and tensile yield strength $\sigma_b = 57.1 \text{ MPa}$. Figure 23 shows the maximum equivalent stress and maximum total deformation of the impeller for different BTEs. It can be seen that the maximum equivalent stress and maximum total deformation of the models with Bezier BTE (M1–10) and the models cutting the SS of the BTE (M13–15) are larger than those of the original model M0, while the models rounding the PS of the BTE (M11 and M12) do not differ much from M0. The maximum equivalent stress of all models is less than 6.5 MPa, which is much lower than the tensile yield strength, and the maximum total deformation of all models is less than 0.065 mm, which is very small compared to the impeller size, therefore the deformation will not affect the pump performance much.

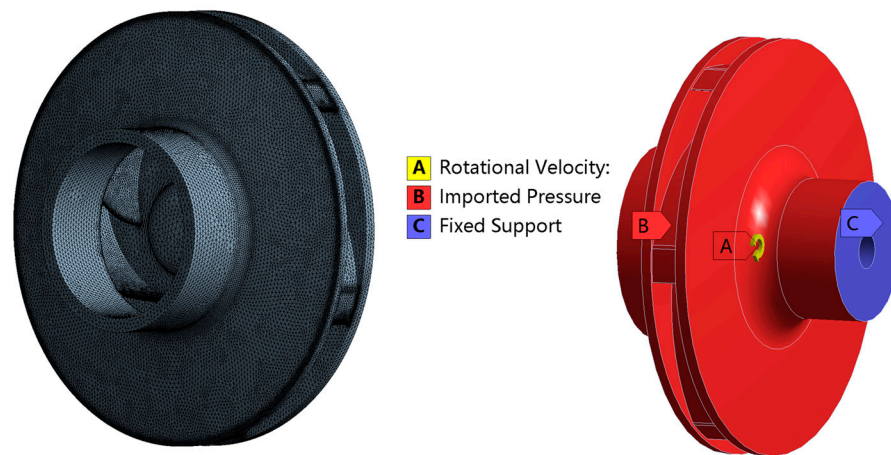


Figure 22. Solid impeller meshes and loading settings.

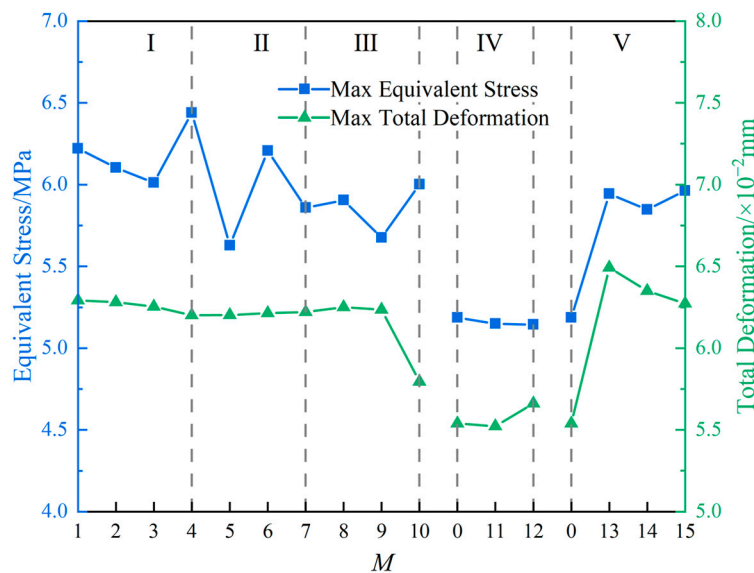
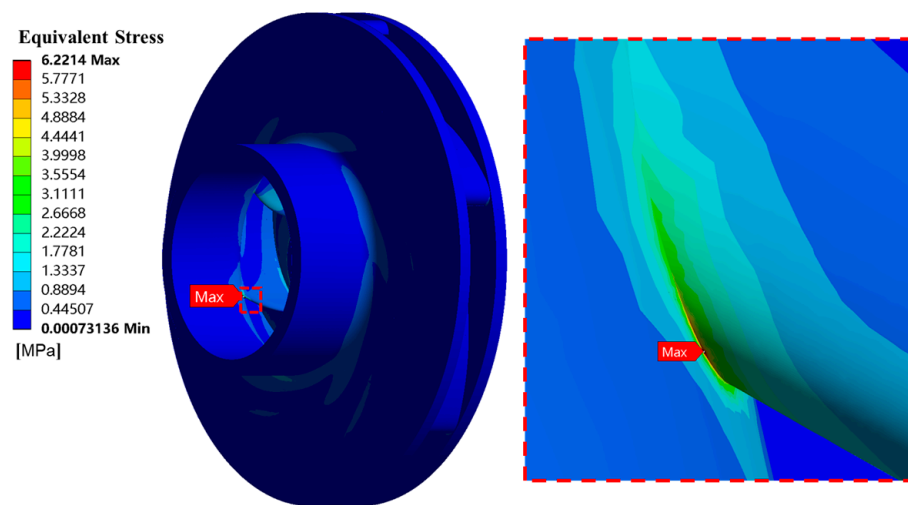
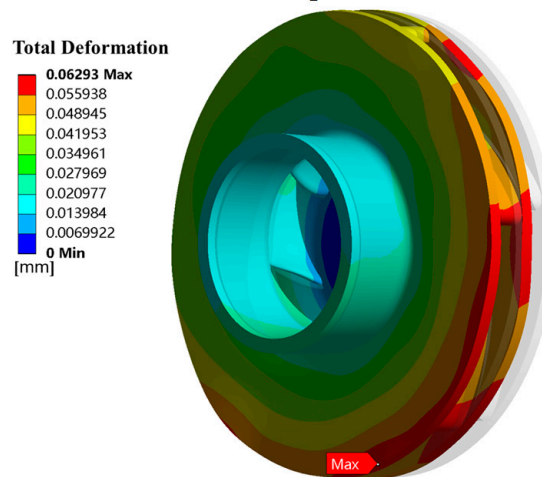


Figure 23. Maximum equivalent stress and maximum total deformation of the impeller for different BTE models.

The maximum equivalent stresses for different BTE models are located at the junction of the blade LE and the shroud, which may be because the blade LE is very thin and a stress concentration is formed near the shroud. The maximum total deformations of different BTE models are located at the maximum diameter of the shroud. Taking M1 as an example, the equivalent stress and total deformation distribution of the impeller are shown in Figure 24.



(a) Distribution of equivalent stress.



(b) Distribution of total deformation.

Figure 24. Distribution of the equivalent stress and total deformation of the impeller for M1.

5. Conclusions

In this paper, the impeller BTE of a centrifugal pump is modified by a Bezier curve, rounding on the PS, and cutting on the SS, and the effects of different BTEs on the performance and internal flow at a rated flow rate are analyzed by numerical simulation. The following conclusions can therefore be drawn:

- (1) The shape of the impeller BTE has an important effect on the performance of the centrifugal pump. Thinning the BTE and connecting it to the blade smoothly can improve pump efficiency; the higher the efficiency, the lower the reverse flow on the impeller outlet.
- (2) Along the BA Streamwise direction, the effect of different BTEs on the reverse flow is mainly reflected in the vicinity of the impeller outlet and diffuser inlet, and there is little effect on the leading part of the impeller. The reverse flow distribution on the impeller outlet along the spanwise direction is large in the middle and small on both sides. The higher the efficiency, the lower the reverse flow distribution on the impeller outlet, and the closer the maximum reverse flow is to the hub.
- (3) Along the BA Streamwise direction, the shaft power of the impeller increases gradually and reaches the maximum when the BA Streamwise = 0.7, and then decreases gradually. Different BTEs have little effect on the shaft power in the leading part of the impeller but have a great effect on the shaft power near the impeller trailing edge.

- (4) Different BTEs have little influence on the energy loss at the leading part of the impeller but have a great influence on energy loss at the impeller outlet and diffuser inlet. Due to the impact effect, the energy loss at the impeller LE has a local maximum. Around the impeller BTE, the energy loss rises sharply due to flow separation and jet-wake structure, reaching a global maximum at the impeller outlet. The energy loss at the diffuser inlet is mainly affected by the energy loss at the impeller outlet; the thicker the impeller BTE, the higher the energy loss at the impeller outlet and diffuser inlet.
- (5) By analyzing the local entropy production rate, it is found that high energy loss is located at the SS of the impeller TE and diffuser LE. Different BTEs have an important effect on entropy production in this region, and thinner BTEs can significantly reduce the entropy production; the closer to the shroud, the higher the entropy production at the impeller LE due to the increase in the relative velocity and impact loss.
- (6) Through the Ω -vortex identification method, it is found that the vortex is mainly located at the impeller inlet, impeller outlet, and diffuser inlet, with the vortex at the impeller outlet being the most affected by different BTEs. Having the thickest BTE, the vortex region and swirling strength of M1 are the greatest. M10 is obtained by thinning the BTE of M1 with a Bezier curve, and M12 is obtained by rounding the PS of the BTE of M0, both of which can reduce the vortex region and swirling strength, making the flow more uniform and lowering the energy dissipation.
- (7) The maximum equivalent stress and maximum total deformation of the impeller in most BTE models are larger than that in the original model M0. The maximum equivalent stress is located at the intersection of the blade LE and the shroud, and the maximum total deformation is located at the maximum diameter of the shroud. The maximum equivalent stress is much less than the tensile yield strength of the material, and the deformation is acceptable.

The present work only studies the influence of different BTEs on steady performance through internal flow analysis, though different BTEs also have an important influence on the unsteady characteristics. In the future, the influence of different BTEs on the unsteady characteristics of pressure pulsation, shaft power, axial force, radial force, and so on should be studied.

Author Contributions: Conceptualization, H.L. and S.W.; methodology, Y.C.; software, Y.Y.; validation, L.B., S.W. and Y.Y.; formal analysis, H.L. and Y.C.; investigation, L.B. and S.W.; resources, Y.C.; data curation, Y.Y.; writing—original draft preparation, H.L.; writing—review and editing, L.Z.; visualization, L.B. and S.W.; supervision, L.Z. and L.B.; project administration, L.Z.; funding acquisition, L.Z. All authors have read and agreed to the published version of the manuscript.

Funding: This research was supported by the National Natural Science Foundation of China (Grant Nos. 52079058 and 52209113) and Nature Science Foundation of Jiangsu Province (Grant No. BK BK20220544).

Institutional Review Board Statement: Not applicable.

Informed Consent Statement: Not applicable.

Data Availability Statement: The data presented in this article are available upon request from the corresponding author.

Conflicts of Interest: The authors declare no conflict of interest.

Nomenclature

BTE	Blade Trailing Edge
CFD	Computational fluid dynamics
GCI	Grid convergence indexes
b_2	Impeller outlet width, mm
D_1	Impeller inlet diameter, mm
D_2	Impeller outlet diameter, mm
H	Head, m
n	Rotate speed, rpm
n_s	Specific speed
P	Shaft power, W
P_{loss}	Energy loss, W
p	Static pressure, Pa
p_t	Total pressure, Pa
Q	Volume flow rate, m ³ /h
Q_{rev}	Reverse flow rate, m ³ /h
Q_{ratio}	Mainstream ratio, %
q	Leakage flow rate through wear ring, m ³ /h
$\dot{S}_{\text{PRO},D}$	Local entropy production rate, W·m ⁻³ ·K ⁻¹
$\dot{S}_{\text{PRO},\bar{D}}$	Local entropy production rate by direct dissipation, W·m ⁻³ ·K ⁻¹
$\dot{S}_{\text{PRO},D'}$	Local entropy production rate by turbulent dissipation, W·m ⁻³ ·K ⁻¹
T	Torque generated by the rotating wall, N·m
V_{uni}	Uniformity of velocity distribution, %
z	Blade number
η	Efficiency, %
ω	Rotate speed, rad/s

References

- Bai, L.; Zhou, L.; Jiang, X.; Pang, Q.; Ye, D. Vibration in a multistage centrifugal pump under varied conditions. *Shock. Vib.* **2019**, *2019*, 2057031. [[CrossRef](#)]
- El-Emam, M.A.; Zhou, L.; Yasser, E.; Bai, L.; Shi, W. Computational Methods of Erosion Wear in Centrifugal Pump: A State-of-the-Art Review. *Arch. Comput. Methods Eng.* **2022**, *29*, 3789–3814. [[CrossRef](#)]
- Rakibuzzaman, M.; Kim, H.; Kim, K.; Suh, S.; Bae, Y. A Study on Booster Pump System with Flow Sensor for Individual Flow Control Method. *J. Appl. Fluid Mech.* **2022**, *15*, 889–900. [[CrossRef](#)]
- Kim, J.H.; Lee, H.C.; Kim, J.H.; Kim, S.; Yoon, J.Y.; Choi, Y.S. Design techniques to improve the performance of a centrifugal pump using CFD. *J. Mech. Sci. Technol.* **2015**, *29*, 215–225. [[CrossRef](#)]
- Gulich, J.F. *Centrifugal Pumps*, 4th ed.; Springer: Cham, Switzerland, 2020.
- Kikuyama, K.; Murakami, M.; Asakura, E.; Osuka, I.; Liu, J. Velocity Distributions in the Impeller Passages of Centrifugal Pumps-Effects of Outlet Edge Shape of the Impeller Blades on the Pump Performance. *Bull. JSME* **1985**, *28*, 1963–1969. [[CrossRef](#)]
- Wu, D.; Yan, P.; Chen, X.; Wu, P.; Yang, S. Effect of Trailing-Edge Modification of a Mixed-Flow Pump. *J. Fluids Eng.* **2015**, *137*, 101205. [[CrossRef](#)]
- Warda, H.; Haddara, S.; Adam, I.G.; Rashad, A.; El-Deen, H.A. Blade Trailing Edge Profile Effect on Low Specific Speed Centrifugal Pump Performance. In Proceedings of the 11th International Conference on the Role of Engineering towards a Better Environment, Alexandria, Egypt, 18–20 December 2017.
- Litfin, O.; Delgado, A.; Haddad, K.; Klein, H.; Asme. Numerical and experimental investigation of trailing edge modifications of centrifugal wastewater pump impellers. In Proceedings of the ASME Fluids Engineering Division Summer Meeting, Waikoloa, HI, USA, 30 July–3 August 2017.
- Yang, J.; Zhou, R.; Chen, H.; Yu, T. Transient flow characteristics and pressure pulsation characteristics at splitter of double-volute centrifugal pump during startup. *J. Jiangsu Univ. Nat. Sci. Edition* **2021**, *42*, 278–283. [[CrossRef](#)]
- Gao, B.; Zhou, Z.; Ni, D.; Zhang, N.; Gu, J. Effects of offset blade on the pressure pulsation and wake structures in a centrifugal pump. *J. Drain. Irrig. Mach. Engineering* **2022**, *40*, 766–770. [[CrossRef](#)]
- Al-Qutub, A.M.; Khalifa, A.E.; Al-Sulaiman, F.A. Exploring the Effect of V-Shaped Cut at Blade Exit of a Double Volute Centrifugal Pump. *J. Press. Vessel Technol.* **2012**, *134*, 021301. [[CrossRef](#)]
- Zhang, N.; Liu, X.; Gao, B.; Wang, X.; Xia, B. Effects of modifying the blade trailing edge profile on unsteady pressure pulsations and flow structures in a centrifugal pump. *Int. J. Heat Fluid Flow* **2019**, *75*, 227–238. [[CrossRef](#)]
- Cui, B.; Zhang, C.; Zhang, Y.; Zhu, Z. Influence of Cutting Angle of Blade Trailing Edge on Unsteady Flow in a Centrifugal Pump Under Off-Design Conditions. *Appl. Sci.* **2020**, *10*, 580. [[CrossRef](#)]

15. Mansour, M.; Thévenin, D.; Parikh, T. Influence of the shape of the impeller blade trailing edge on single and two-phase airwater flows in a centrifugal pump. In Proceedings of the Proceedings of the 36th International Pump Users Symposium, Houston, TX, USA, 13–16 December 2020.
16. Lin, Y.; Li, X.; Li, B.; Jia, X.; Zhu, Z. Influence of Impeller Sinusoidal Tubercle Trailing-Edge on Pressure Pulsation in a Centrifugal Pump at Nominal Flow Rate. *J. Fluids Eng.* **2021**, *143*, 091205. [[CrossRef](#)]
17. Lin, Y.; Li, X.; Zhu, Z.; Wang, X.; Lin, T.; Cao, H. An energy consumption improvement method for centrifugal pump based on bionic optimization of blade trailing edge. *Energy* **2022**, *246*, 123323. [[CrossRef](#)]
18. Qian, B.; Wu, P.; Huang, B.; Zhang, K.; Li, S.; Wu, D. Optimization of a Centrifugal Impeller on Blade Thickness Distribution to Reduce Hydro-Induced Vibration. *J. Fluids Eng.* **2020**, *142*, 021202. [[CrossRef](#)]
19. Ji, L.; Li, W.; Shi, W.; Tian, F.; Agarwal, R. Effect of blade thickness on rotating stall of mixed-flow pump using entropy generation analysis. *Energy* **2021**, *236*, 121381. [[CrossRef](#)]
20. Wu, C.; Zhang, W.; Wu, P.; Yi, J.; Ye, H.; Huang, B.; Wu, D. Effects of Blade Pressure Side Modification on Unsteady Pressure Pulsation and Flow Structures in a Centrifugal Pump. *J. Fluids Eng.* **2021**, *143*, 111208. [[CrossRef](#)]
21. Wu, C.; Pu, K.; Li, C.; Wu, P.; Huang, B.; Wu, D. Blade redesign based on secondary flow suppression to improve energy efficiency of a centrifugal pump. *Energy* **2022**, *246*, 123394. [[CrossRef](#)]
22. Tharwat, A.; Elhoseny, M.; Hassani, A.E.; Gabel, T.; Kumar, A. Intelligent Bézier curve-based path planning model using Chaotic Particle Swarm Optimization algorithm. *Clust. Comput.* **2018**, *22*, 4745–4766. [[CrossRef](#)]
23. Song, B.Y.; Wang, Z.D.; Zou, L. An improved PSO algorithm for smooth path planning of mobile robots using continuous high-degree Bezier curve. *Appl. Soft Comput.* **2021**, *100*, 106960. [[CrossRef](#)]
24. Gardner, B.; Selig, M. Airfoil design using a genetic algorithm and an inverse method. In Proceedings of the 41st Aerospace Sciences Meeting and Exhibit, Reno, NV, USA, 6–9 January 2003; p. 43.
25. Nanthini, R.; Prasad, B.V.S.S.S.; Sanyasiraju, Y.V.S.S. Effect of Bezier control points on blade pressure distribution. In Proceedings of the Advanced Trends in Mechanical and Aerospace Engineering, Bangalore, India, 7–9 November 2019.
26. Yang, Y.; Zhou, L.; Hang, J.; Du, D.; Shi, W.; He, Z. Energy characteristics and optimal design of diffuser meridian in an electrical submersible pump. *Renew. Energy* **2021**, *167*, 718–727. [[CrossRef](#)]
27. Li, H.; Han, Y.; Shi, W.; Tiganik, T.; Zhou, L. Automatic optimization of centrifugal pump based on adaptive single-objective algorithm and computational fluid dynamics. *Eng. Appl. Comput. Fluid Mech.* **2022**, *16*, 2221–2241. [[CrossRef](#)]
28. Rakibuzzaman, M.; Suh, S.-H.; Kim, H.-H.; Ryu, Y.; Kim, K.Y. Development of a Hydropower Turbine Using Seawater from a Fish Farm. *Processes* **2021**, *9*, 266. [[CrossRef](#)]
29. Roache, P.J. Perspective: A method for uniform reporting of grid refinement studies. *J. Fluids Eng.* **1994**, *116*, 405–413. [[CrossRef](#)]
30. Celik, I.B.; Ghia, U.; Roache, P.J.; Freitas, C.J. Procedure for estimation and reporting of uncertainty due to discretization in CFD applications. *J. Fluids Eng.-Trans. Asme* **2008**, *130*, 078001. [[CrossRef](#)]
31. Bardina, J.; Huang, P.; Coakley, T.; Bardina, J.; Huang, P.; Coakley, T. Turbulence modeling validation. In Proceedings of the 28th Fluid Dynamics Conference, Snowmass Village, CO, USA, 29 June–2 July 1997; p. 2121.
32. Wang, K.; Ju, Y.; Zhang, C. A Quantitative Evaluation Method for Impeller-Volute Tongue Interaction and Application to Squirrel Cage Fan With Bionic Volute Tongue. *J. Fluids Eng.* **2019**, *141*. [[CrossRef](#)]
33. Han, Y.; Zhou, L.; Bai, L.; Shi, W.; Agarwal, R. Comparison and validation of various turbulence models for U-bend flow with a magnetic resonance velocimetry experiment. *Phys. Fluids* **2021**, *33*, 125117. [[CrossRef](#)]
34. ISO 9906:2012(E); Rotodynamic Pumps—Hydraulic Performance Acceptance Tests—Grades 1, 2 and 3. International Organization for Standardization: Geneva, Switzerland, 2012.
35. Wang, C.Y.; Wang, F.J.; Zou, Z.C.; Xiao, R.F.; Yang, W. Effect of lean mode of blade trailing edge on hydraulic performance for double-suction centrifugal pump. *IOP Conf. Ser. Earth Environ. Sci.* **2019**, *240*, 032030. [[CrossRef](#)]
36. Li, D.; Wang, H.; Qin, Y.; Han, L.; Wei, X.; Qin, D. Entropy production analysis of hysteresis characteristic of a pump-turbine model. *Energy Convers. Manag.* **2017**, *149*, 175–191. [[CrossRef](#)]
37. Kock, F.; Herwig, H. Local entropy production in turbulent shear flows: A high-Reynolds number model with wall functions. *Int. J. Heat Mass Transf.* **2004**, *47*, 2205–2215. [[CrossRef](#)]
38. Herwig, H.; Kock, F. Direct and indirect methods of calculating entropy generation rates in turbulent convective heat transfer problems. *Heat Mass Transf.* **2006**, *43*, 207–215. [[CrossRef](#)]
39. Kock, F.; Herwig, H. Entropy production calculation for turbulent shear flows and their implementation in cfd codes. *Int. J. Heat Fluid Flow* **2005**, *26*, 672–680. [[CrossRef](#)]
40. Zhou, L.; Hang, J.; Bai, L.; Krzemianowski, Z.; El-Emam, M.A.; Yasser, E.; Agarwal, R. Application of entropy production theory for energy losses and other investigation in pumps and turbines: A review. *Appl. Energy* **2022**, *318*, 119211. [[CrossRef](#)]
41. Mosallem, M.M. Numerical and experimental investigation of beveled trailing edge flow fields. *J. Hydrodyn.* **2008**, *20*, 273–279. [[CrossRef](#)]
42. Do, T.; Chen, L.; Tu, J. Numerical study of turbulent trailing-edge flows with base cavity effects using URANS. *J. Fluids Struct.* **2010**, *26*, 1155–1173. [[CrossRef](#)]
43. Liu, C.; Gao, Y.; Dong, X.; Wang, Y.; Liu, J.; Zhang, Y.; Cai, X.; Gui, N. Third generation of vortex identification methods: Omega and Liutex/Rortex based systems. *J. Hydrodyn.* **2019**, *31*, 205–223. [[CrossRef](#)]

44. Liu, C.; Wang, Y.; Yang, Y.; Duan, Z. New omega vortex identification method. *Sci. China Phys. Mech. Astron.* **2016**, *59*, 684711. [[CrossRef](#)]
45. Spurk, J.H.; Aksel, N. *Fluid Mechanics*, 2nd ed.; Springer: Berlin/Heidelberg, Germany, 2008.
46. Yao, T.; Zheng, Y. Finite element analysis of stress, deformation and modal of head cover in axi-al-flow hydro-turbine. *J. Drain. Irrig. Mach. Eng.* **2020**, *38*, 39–44. [[CrossRef](#)]

Disclaimer/Publisher's Note: The statements, opinions and data contained in all publications are solely those of the individual author(s) and contributor(s) and not of MDPI and/or the editor(s). MDPI and/or the editor(s) disclaim responsibility for any injury to people or property resulting from any ideas, methods, instructions or products referred to in the content.